Biophysical Journal
Article

Biophysical Society

Probing Mitotic CENP-E Kinesin with the Tethered Cargo Motion Assay and Laser Tweezers

Nikita Gudimchuk,[1,2,3] Ekaterina V. Tarasovetc,[1] Vadim Mustyatsa,[4] Alexei L. Drobyshev,[3] Benjamin Vitre,[5] Don W. Cleveland,[5] Fazly I. Ataullakhanov,[2,3,4,*] and Ekaterina L. Grishchuk[1,*]
[1]Department of Physiology, Perelman School of Medicine, University of Pennsylvania, Philadelphia, Pennsylvania; [2]Department of Physics, Moscow State University, Moscow, Russia; [3]Center for Theoretical Problems of Physicochemical Pharmacology, Russian Academy of Sciences, Moscow, Russia; [4]Dmitry Rogachev National Research Centre of Pediatric Hematology, Oncology and Immunology, Moscow, Russia; and [5]Ludwig Institute for Cancer Research and Department of Cellular and Molecular Medicine, University of California, San Diego, La Jolla, California

ABSTRACT Coiled-coil stalks of various kinesins differ significantly in predicted length and structure; this is an adaption that helps these motors carry out their specialized functions. However, little is known about the dynamic stalk configuration in moving motors. To gain insight into the conformational properties of the transporting motors, we developed a theoretical model to predict Brownian motion of a microbead tethered to the tail of a single, freely walking molecule. This approach, which we call the tethered cargo motion (TCM) assay, provides an accurate measure of the mechanical properties of motor-cargo tethering, verified using kinesin-1 conjugated to a microbead via DNA links in vitro. Applying the TCM assay to the mitotic kinesin CENP-E unexpectedly revealed that when walking along a microtubule track, this highly elongated molecule with a contour length of 230 nm formed a 20-nm-long tether. The stalk of a walking CENP-E could not be extended fully by application of sideways force with optical tweezers (up to 4 pN), implying that CENP-E carries its cargo in a compact configuration. Assisting force applied along the microtubule track accelerates CENP-E walking, but this increase does not depend on the presence of the CENP-E stalk. Our results suggest that the unusually large stalk of CENP-E has little role in regulating its function as a transporter. The adjustable stalk configuration may represent a regulatory mechanism for controlling the physical reach between kinetochore-bound CENP-E and spindle microtubules, or it may assist localizing various kinetochore regulators in the immediate vicinity of the kinetochore-embedded microtubule ends. The TCM assay and underlying theoretical framework will provide a general guide for determining the dynamic configurations of various molecular motors moving along their tracks, freely or under force.

INTRODUCTION

A mechanistic understanding of motor-cargo interactions at the single-molecule level is crucial for unraveling the complexities of intracellular transport and engineering motile biomimetic devices. Members of the kinesin superfamily of ATP-dependent motors contribute to specialized transport functions in cells, moving various cargo along intracellular microtubule (MT) tracks (1). These functions are assisted by the coiled-coil domains, or stalks, which ensure homodimerization and often have additional roles (2,3). There is marked variability in the length and structure of stalk domains; accordingly, they are likely to form MT-cargo tethers with diverse mechanical and conformational properties. For example, the stalk of the highly processive kinesin-8 Kif18a is formed by a ~12 nm coiled-coil domain (4), whereas the major transport motor kinesin-1 has two coiled-coil regions separated by a hinge, with a total contour length of ~80 nm (5). The relationship between the secondary structure of the stalk and the conformational and mechanical properties of the tether it provides for cargo attachment is not well understood. Kinesin-1, for example, is estimated to form a 17 or 57 nm tether, based on two separate studies (6,7), and apparently its stalk becomes fully extended under a very low force (<1 pN) (8).

Even less is known about the conformation of the actively walking CENP-E, a mitotic kinesin. Defects in this motor are associated with chromosome segregation errors, aneuploidy, and the development of tumors (9–11).

Submitted October 18, 2017, and accepted for publication April 10, 2018.

*Correspondence: ataullakhanov.fazly@gmail.com or gekate@pennmedicine.upenn.edu

Nikita Gudimchuk and Ekaterina V. Tarasovetc contributed equally to this work.

Benjamin Vitre's present address is CRBM, CNRS, University of Montpellier, Montpellier, France.

Editor: Steven Rosenfeld.

https://doi.org/10.1016/j.bpj.2018.04.017

This kinesin-7 subfamily member has an unusually long stalk of 200–230 nm in contour length (12). The highly discontinuous coiled-coil structure of the stalk implies that it is flexible, with an estimated persistence length (PL) of only 26 nm (13). Because the C-terminal tail of CENP-E is likely to be disordered (14), when fully extended this region could add another ~80 nm to the total contour length. The tail of CENP-E contains an MT-binding site, although its exact location within the tail is not known (13,15). A CENP-E tail fragment containing an MT-binding site diffuses very rapidly along the MT lattice with an average binding time of <0.5 s, indicating relatively weak MT-binding affinity (13). This site plays an essential role in enabling CENP-E to track the ends of dynamic MTs bidirectionally and processively in vitro, likely contributing to the stability of kinetochore-MT attachments during mitosis. The exact cellular role of the highly elongated CENP-E stalk, however, remains unknown. In the absence of external load, full-length (FL) CENP-E and a truncated (TR) construct with no tail or stalk have very similar transport rates and run lengths in vitro (13). Strikingly, a significantly shortened stalk severely disrupts CENP-E functioning in mitotic cells (16). Therefore, a quantitative understanding of the conformational properties of walking CENP-E as well as how its extension length changes under load is crucial for deciphering its mitotic function.

Despite substantial advances in fluorescence-based imaging techniques, it is not currently possible to visualize the length and conformation of tethering formed by cargo-transporting motors. Notably in this regard, tracking of a microbead transported along the MTs by molecular motor can reveal basic mechanical features of motor-driven movements (17,18). At the same time, single-particle tracking of the Brownian motion of a microbead tethered to a fixed point provides a powerful tool for gauging the mechanical and conformational properties of the underlying tether. This tethered particle motion (TPM) assay has been successfully used to study the length and flexibility of double-stranded (ds) DNA (19–23) and to analyze DNA looping and the interactions between nucleic acid chains and proteins in real time (23–27). A similar approach, the tethered fluorophore motion assay (28), has recently been used to measure the flexural stiffness of single myosin motors stably attached to actin filaments (29). To further adapt these quantitative approaches to moving motors, we constructed and critically analyzed a theoretical model that describes the Brownian motion of a bead carried by a motor stepping with variable velocity on different protofilament tracks of a coverslip-attached MT. We deduced the relationship between the extent of bead excursions and the bead's tethering and verified it experimentally using a kinesin-1 motor fastened to a microbead by double-stranded DNA (dsDNA) links of known lengths. Unexpectedly, applying the TCM approach to CENP-E kinesin revealed that this motor is not extended to its full contour length when it is walking freely or under a sideways-pulling force applied by laser tweezers. The compact configuration, however, does not change the load-bearing properties of the CENP-E motor, strongly suggesting that the primary role of the CENP-E stalk during chromosome segregation is regulatory rather than mechanical in nature.

MATERIALS AND METHODS

Experimental procedures

Protein construction and purification

Tubulin was purified from cow brains by thermal cycling and chromatography (30) and then labeled with rhodamine (31). TR kinesin-1 construct labeled with GFP (K560) and TR and FL CENP-E kinesins were purified as in (12,32). SNAP-GBP construct was prepared by fusing the gene for GBP-6His tag (33) in frame with the SNAP-tag (New England Biolabs (NEB), Ipswich, MA), separated by the flexible linker SGGGGSGGGG in pET28a (Novagen, Madison, WI). Expression was induced at 37°C for 2 h with 1 mM isopropyl β-D-1-thiogalactopyranoside in NEB Express *E. coli* cells; bacterial pellets were lysed with lysozyme (1 mg ml^{-1}) on ice for 30 min and sonicated in a buffer containing 50 mM NaH_2PO_4 (pH 8.0), 300 mM NaCl, 10 mM imidazole, and 1% phenylmethylsulfonyl fluoride. After centrifugation at 10,000 × *g* for 20 min, supernatant was incubated with Ni-nitrilotriacetic acid agarose (Qiagen, Hilden, Germany) for 1 h at 4°C. Bound protein was eluted with 250 mM imidazole, loaded onto a Dispo-Biodialyzer unit (pore size 10 kDa molecular weight cutoff; Sigma-Aldrich, St. Louis, MO), and dialyzed in a buffer containing 50 mM NaH_2PO_4 (pH 8.0), 300 mM NaCl, 1 mM dithiothreitol (DTT), and 0.1% Tween-20. Protein fractions were supplemented with 50% glycerol, aliquoted, snap-frozen in liquid N_2, and stored at −80°C.

dsDNA links

Oligonucleotides and primers labeled with biotin or an amino group were purchased from Integrated DNA Technology (Coralville, IA). Amino-group-labeled oligonucleotides were conjugated with benzylguanine (BG) (NEB), as described (34). Short dsDNA links were prepared by complementary pairing of 1 μM biotin-labeled and 5 μM BG-labeled oligonucleotides at room temperature for 1 h in 5× phosphate-buffered saline (PBS) (700 mM NaCl, 13.5 mM KCl, 50.5 mM Na_2HPO_4, 9 mM KH_2PO_4, (pH 7.2)). Long dsDNA links were prepared by polymerase chain reaction (PCR) using one primer labeled with biotin and a second primer labeled with BG, plasmid pET21a as template, and FastStartTaq DNA polymerase (Roche, Basel, Switzerland). The PCR product was purified using the QIAquick PCR Purification kit (Qiagen), diluted to 1 μM in MilliQ H_2O, and stored as aliquots at −20°C. Sequences of PCR primers and the resultant dsDNA are provided in Supporting Materials and Methods.

Preparation of beads coated with kinesin-1 and dsDNA links

Neutravidin was conjugated to 0.5 μm COOH-activated glass beads (Bangs Labs, Fishers, IN), as described (35). Beads were incubated with biotinylated dsDNA (concentrations provided below) in 5× PBS for 2 h, washed extensively by centrifugations at 2600 × *g*, blocked with 250 μM biotinylated discrete polyethylene glycol (2.5 kDa; Quanta BioDesign, Plain City, OH), and resuspended in 1× PBS containing 4 mg mL^{-1} bovine serum albumin (BSA) and 2 mM DTT. SNAP-GBP protein (5 μM) was attached to these beads via a covalent bond with dsDNA-bound BG by incubation for 1.5 h at 4°C. Beads were washed three times and stored at −20°C in PBS with 4 mg mL^{-1} BSA, 2 mM DTT, and 50% glycerol. Before each experiment, the beads were washed in BRB80 buffer (80 mM 1,4-Piperazinediethanesulfonic acid (pH 6.9), 4 mM $MgCl_2$, 1 mM EGTA) supplemented with 10 μM Mg-ATP, 2 mM DTT, and 4 mg mL^{-1} BSA; incubated in the same buffer for 1.5–2 h with K560 protein (32); washed; and then used immediately. The amount of dsDNA (per 1 mg of beads) was 2.1–2.8 pmol in group 1, 0.35–1.4 pmol in group 2, 70 pmol in group 3, and 1.4–1.75 pmol in group 4. The amount of K560 was 0.04 pmol in groups 1–3 and 0.4 pmol in group 4. The resultant difference in density of bead coating was confirmed by measurement of bead brightness in the GFP channel and by quantifying the fraction of moving beads; beads with the dense motor coatings were brighter and moved on MTs more frequently (Fig. S4 *a*).

Preparation of CENP-E-coated beads

We coated 0.5 μm COOH-activated glass beads (Bangs Labs) with streptavidin or neutravidin, as described (35). TR CENP-E kinesin was conjugated by first incubating these beads with biotinylated anti-6His antibody (Abcam, Cambridge, UK) in PBS containing 4 mg mL^{-1} BSA and 2 mM DTT. The beads were then blocked with 250 μM biotinylated discrete polyethylene glycol, washed extensively, and incubated with TR CENP-E for 2–4 h at 4°C in BRB80 with 100 μM Mg-ATP, 2 mM DTT, and 4 mg mL^{-1} BSA. Washed beads were kept on ice; before each experiment, beads were sonicated for 3–5 min to reduce clumping. FL CENP-E beads were prepared and used analogously. This protein was conjugated via biotinylated anti-GFP antibodies (Rockland Immunochemicals, Limerick, PA) using the same protocol as for TR CENP-E or a similar procedure described in (13). These methods produced indistinguishable results in the tethered cargo motion (TCM) assay, so small-bead excursions were unlikely to be caused by the CENP-E stalk sticking to the beads. Moreover, CENP-E binding to the beads was specific, as almost no binding was seen in the absence of the antibodies (Fig. S5, *b* and *c*). To ensure that beads were predominantly transported by single CENP-E motors, the density of CENP-E coating was reduced until a majority of the beads did not move; only chambers with $<$30% moving beads were analyzed (7,36). Run lengths of such beads (Fig. S5 *d*) were consistent with previously published values for single CENP-E molecules (13,37).

TCM experimental procedures

Flow chambers were prepared using silanized coverslips and double-sided tape, and solutions were exchanged with a peristaltic pump, as described (38). All assays were performed at 32°C. Taxol-stabilized MTs, polymerized from a mixture containing nine parts of unlabeled tubulin (11 mg mL^{-1}) and one part of rhodamine-labeled tubulin (degree of labeling 0.9; 6 mg mL^{-1}) were immobilized on the coverslip via antitubulin antibodies (Serotec, Hercules, CA). Coverslips were blocked with 1% pluronic F127, and beads were introduced in motility buffer: 80 mM K-1,4-Piperazinediethanesulfonic acid (pH 6.9), 1 mM EGTA, 1–4 mM MgCl$_2$, 4 mg mL^{-1} BSA, 2 mM DTT, 6 mg mL^{-1} glucose, 80 μg mL^{-1} catalase, 0.1 mg mL^{-1} glucose oxidase, 0.5% β-mercaptoethanol, 7.5 μM taxol, and Mg-ATP. CENP-E bead motility was assayed at 2 mM Mg-ATP, and kinesin-1 was assayed at 30 or 400 μM Mg-ATP to slow the motor down and collect better statistics. Bead MT-perpendicular excursions did not significantly differ at 30 and 400 μM Mg-ATP (Fig. S4 *b*), so these data were combined. Less than one-third of beads (groups 1–3) moved along MTs in our experiment.

Our laser-trap instrument has been described previously (39). Some experiments used the upgraded version of this microscopy system, described in (40). With a 1064 nm laser beam (stiffness 0.0025 pN nm^{-1}), a free-floating bead was trapped, brought into contact with an MT, and kept there for 80 s. If directed motion was observed, the trap was switched off immediately, and video recording with differential interference contrast (DIC) was performed using stream acquisition mode (10 ms exposure) using a Photometrics Cascade 650 charge-coupled device camera. In addition, an MT image was taken in the rhodamine channel with 300 ms exposure for subsequent analysis of bead excursions relative to the MT.

Force-clamp and sideways-force experiments

The force clamp was implemented via a feedback control of piezo-stage P-561.3D (Physik Instrumente, Karlsruhe, Germany). A custom-made LabVIEW program triggered the force-clamp regime in response to bead displacement greater than 150 nm from the trap's center, as detected by a quadrant photodetector (QPD) sampled at 4 kHz and decimated before recording. Laser-trap stiffness was varied (0.008–0.03 pN nm^{-1}) to apply force in a range of 0.1–6 pN. Beads were additionally imaged in DIC to measure displacements beyond the working range of QPD. The piezo stage was controlled at 100 Hz with a feedback coefficient of 0.3–0.5 to maintain constant distance between the centers of the trap and microbead. The MT was recorded with DIC before each experiment, and its orientation relative to the stage axes was measured and used as an input for the force-clamp program. For each bead, optical-trap stiffness calibrations were conducted as in (40) at the end of each experiment. Stage and bead coordinates were recorded at 400 Hz and analyzed using a custom-made MATLAB (The MathWorks, Natick, MA) code. The sideways-force assay was conducted essentially in the same manner as that of the force-clamp assay, except that after the ~1 pN opposing force was applied, an acoustooptic deflector was additionally used to steer the trap at 1 Hz perpendicular to the MT with an amplitude of 1 μm; laser-trap stiffness was 0.02–0.04 pN nm^{-1}. The fast detachment of CENP-E-coated beads under load prevented us from examining sideways forces larger than 4 pN.

Data analyses

Analysis of experimental TCM data

To extract bead coordinates, recorded stacks of DIC images were tracked using Metamorph (Molecular Devices, San Jose, CA). Bead coordinates were plotted in the *X*/*Y* plane using custom-written MATLAB code. The corresponding fluorescence MT image was then used to determine the angle between the MT and *X* axis in the image plane. A line representing the MT with the same angle was drawn on the *X*/*Y* plane such that the average deviation of the bead coordinates from this line was minimal. This procedure was introduced because it was not possible to accurately overlay the DIC and fluorescent channels. The MT-perpendicular bead excursions from the MT-representing line were then calculated for each time point, and the resultant distribution was fitted with a Gaussian function to determine its SD. To estimate variation in this SD value, bootstrapping was performed using a custom-made MATLAB code with 30 independent bootstrap samples; data points from all beads for each tether investigated were pulled together, and 300 random data points were drawn with replacement to calculate SD of Gaussian fit's SD. To compensate for "blurring" of the bead's image during camera exposure, the SDs of bead excursions were divided by 0.7, which was the experimentally measured correction factor (see Supporting Materials and Methods). Two-dimensional "cloud" plots were constructed as described in Supporting Materials and Methods.

Analysis of CENP-E displacement during sideways-bead oscillations

Data from the QPD, video recordings with the charge-coupled device camera, and piezo-stage displacement data were analyzed using the MATLAB program. Signals were aligned based on a distinct 1 Hz periodicity introduced by the sideways sweeping of the bead. Bead detachment events were evident from a sudden increase in the oscillation amplitude up to 1 μm and a simultaneous change in the direction of stage motion, indicating disruption of the feedback loop. The sideways force *F* acting on the bead at each time point was calculated as follows, taking into account the nonlinearity of the optical trap stiffness at large bead displacements (41):

$$F = k \cdot \Delta y' \cdot e^{-\frac{(\Delta y')^2}{2 \cdot R^2}}, \tag{1}$$

where *k* is the trap stiffness at the center of the trap, $\Delta y' = y'_{bead} - y'_{trap}$ is the distance between the bead and trap centers, and R = 250 nm is the bead radius.

We took into account the specific geometry of the system (Fig. S5 *e*) to determine the distance D between the bead surface and the MT for each bead position:

$$D = \sqrt{y'^2_{bead} + R^2} - R. \quad (2)$$

The height of the MT, which is much smaller than R, was neglected. During sweeping, the bead was assumed to remain at a constant distance from the coverslip because changes in the z-position of the laser trap moving 1 μm in the imaging plane are negligible.

Analysis of the force-velocity and force-detachment curves

At saturating ATP concentration, the dependence of motor velocity V on external force F was fitted as follows (42):

$$V(F) = d \bullet k_{cat} = \frac{d \bullet k_o}{p + q \bullet e^{-\frac{F \bullet \delta}{k_B \bullet T}}}. \quad (3)$$

Here, $d = 8$ nm is the size of a single step of kinesin, k_{cat} is the catalytic rate constant, k_o is the unloaded rate constant, k_B is the Boltzmann constant, T is the temperature, δ is the characteristic distance over which the load acts, and p and $q = (1-p)$ are the fractions of the unloaded catalytic cycle required for the biochemical and mechanical transitions, respectively. The stalling force was determined using linear fit in the range of −4 to 2 pN.

The dependence of CENP-E kinesin attachment time on applied force was fitted to the following symmetrical exponential function (43):

$$T(F) = T_o \bullet e^{-\left|\frac{F}{F_d}\right|}. \quad (4)$$

Here, T_o is the attachment time of CENP-E kinesin to the MT in the absence of external load, and F_d is the detachment force.

Theoretical modeling

Simulation of bead-fluctuation dynamics

We simulated the MT as a 25 nm cylinder lying on the surface of a plane representing the coverslip. The bead-MT tether was modeled as a worm-like chain of 2 nm segments. The last point of the chain was anchored at the surface of a bead sphere with a radius of 250 nm. This connection was allowed significant flexibility by selecting rotation angles from a Gaussian distribution with SD = 17°. The first chain segment was anchored at the MT surface, and this site coincided with the position of a motor. Orientation of the first segment was fixed perpendicularly to the MT surface. Additional calculations showed that introducing greater rotational mobility of the MT-anchored segment of the chain and the chain's self-avoidance did not affect major model predictions (see Supporting Materials and Methods; Fig. S1 *c*). The position of all other chain segments was calculated at each time by randomly selecting the angle at which the next segment deflects from the previous segment from a Gaussian distribution. The variance of this distribution was chosen to provide the desired PL of the chain. Monte Carlo simulations of the "tether-bead" system were carried out as in (21) using a coordinate system in which the motor was stationary. All configurations in which the coordinates of at least one chain segment were found within the bead, MT, or coverslip were discarded. This rule ensured that the tether did not penetrate into these objects. Likewise, configurations in which the bead overlapped with the coverslip were discarded. The presence of the coverslip and bead constrains increases the end-to-end distance of the tether. For example, the 230 nm tether with PL = 26 nm has end-to-end distance 97 ± 1 nm (mean ± SEM, N = 2000) when the tether is modeled with no bead, coverslip or MT, but this distance increases up to 125 ± 1 nm in a system containing all these components. Simulations were implemented using a custom program written in MATLAB (available upon request). Additional details are provided in Supporting Materials and Methods.

RESULTS

Theoretical framework for TCM analysis of a walking motor

We used a theoretical approach to establish a quantitative framework for analysis of the conformational properties of motor-cargo tethering. Using Monte Carlo simulations, we modeled the motions of microbeads attached via mechanically different tethers to a motor walking along an MT track located in the plane of a coverslip (Fig. 1, *a* and *b*; Videos S1 and S2). In the traditional TPM assay, the Brownian motion of a tethered microbead is analyzed relative to the point of the tether's attachment to the coverslip surface (19–23). We modified this approach to incorporate two specific features of the motor-MT system. First, to take into account the fact that the kinesin motor walks processively and unidirectionally, Brownian bead motion was analyzed relative to a system of coordinates centered at the moving kinesin (Fig. 1, *c* and *d*). The second complexity of the TCM system is that the coverslip-attached MT cylinder provides multiple protofilament tracks for kinesin binding and walking. Because of steric hindrance, the motor binds with different probabilities to different MT protofilaments (Fig. S1). Moreover, when the motor walks along different MT protofilaments, the range and average angle of the kinesin-coupled bead excursions are sterically restricted to different degrees, as illustrated by Figs. S2 and S3. Therefore, experimental results obtained with multiple beads and MTs should correspond to the average behavior on different protofilaments. To accurately represent these complexities in our model, bead coordinates calculated for different protofilaments were averaged using weight coefficients corresponding to the likelihood that the motor would land on a given protofilament (see Supporting Materials and Methods).

Using this modeling framework, we calculated the predicted range of bead excursions as a function of the length of a mobile tethering molecule. The SD of bead excursions increases nonlinearly with increasing contour length (Fig. 1 *e*). For flexible tethers, such as the discontinuous coiled-coil stalk of CENP-E (PL = 26 nm (13)) and dsDNA (PL = 46 nm (44)), the SD dependence is best described by a polynomial function of fractional powers. With increasing tether stiffness (e.g., for PL = 150 nm, as in a continuous coiled-coil stalk (45)), this dependence becomes more linear. These calculations reveal the relatively modest impact of tether stiffness within the physiological range of the stalk lengths. Consistent with the theoretical findings in (46), the tether's stiffness plays more prominent role when the tether length is increased (Fig. S1 *c*). Importantly, these data show that the range of bead excursions can accurately report the length of

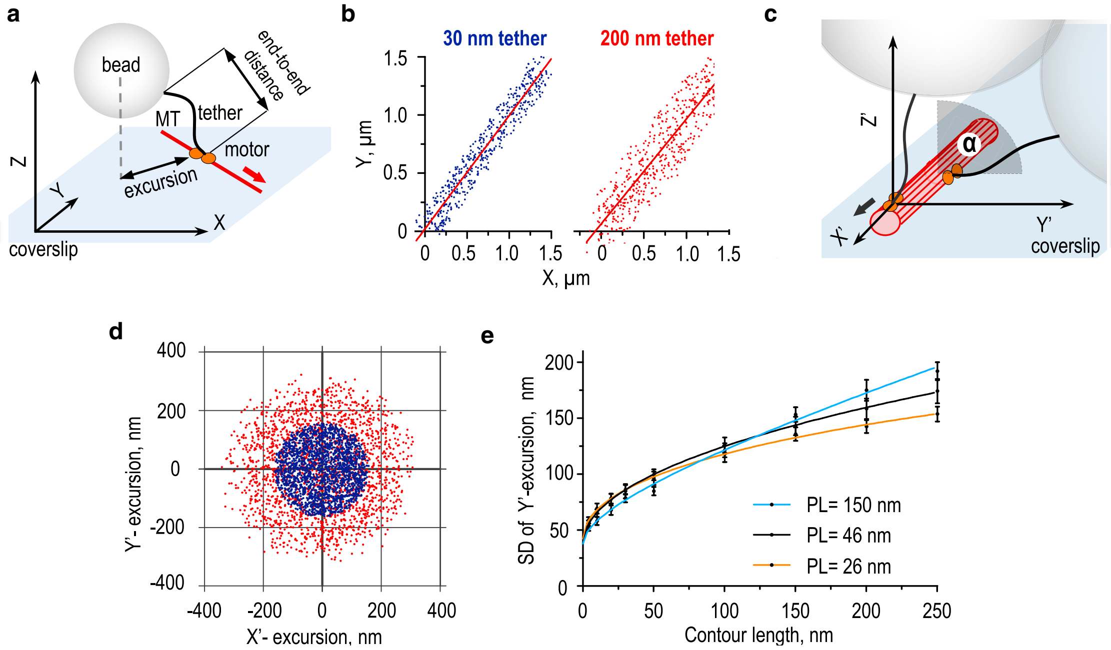

FIGURE 1 Theoretical predictions for the TCM assay. (*a*) A schematic of the in vitro motility assay is shown, which uses 0.5 μm beads conjugated to the MT-dependent motor molecule via its natural tail extension or an artificial elongated link. The MT is immobilized on the coverslip; the red arrow indicates the direction of motor walking in the stationary coordinate system *XYZ*. (*b*) Predicted *XY* coordinates are shown for the bead moving on top of the MT at 20 μm min^{-1} in the stationary coordinate system (500 coordinates for each tether with PL = 46 nm). Lines representing MTs are shown in dark red. (*c*) A schematic of motor-MT attachment in the moving system of coordinates is shown. Axis *X'* points along the MT in the direction of motor walking (*black arrow*), *Y'* and *Z'* are perpendicular to the MT, and the origin is located on the surface of the MT at the attachment site for motor domains. Two example attachments to different protofilament tracks are shown. Angle α measures the position of the walking motor relative to the protofilament on top of the MT, for which $\alpha = 0°$. (*d*) Two-dimensional "cloud" plots show the predicted bead excursions for 30 nm (*blue*) and 200 nm (*red*) tethers in the moving coordinate system. Data are for $\alpha = 0°$; there is a total of 2000 points for each tether with PL = 46 nm. (*e*) The predicted relationship between the SD of MT-perpendicular bead excursions along the *Y'*-axis (*Y'*-excursion) and contour lengths for different tethers are shown. The lines are empirical fits with the following functions: $a + bx + cx^{0.5}$. Data for each tether is based on n = 9000 coordinates. Error bars (SD) were generated by bootstrap analysis; see Materials and Methods. To see this figure in color, go online.

a bead tether. Thus, Brownian motion of tethered cargo can be used to gauge the conformational properties of tethering formed by a walking kinesin motor. Accordingly, we called this quantitative method the TCM approach.

Experimental verification of the TCM approach using kinesin-1 with variable dsDNA links

To test these theoretical predictions, we developed an in vitro motility assay to directly measure excursions of a microbead tethered to a kinesin-1 motor via links of known lengths. We designed two dsDNAs of 34 and 557 bp, representing short (12 nm) and long (189 nm) links, respectively. One end of the dsDNA was attached to a 500 nm silica bead via biotin-neutravidin chemistry (Fig. 2 *a*; see Materials and Methods). The opposite 5′-DNA end was modified to add BG, a substrate for the SNAP (47) enzyme. The BG-labeled dsDNA was then covalently attached to a specially designed protein adaptor, in which SNAP was fused to GBP, a nanobody derived from camelid antibody fragment (48). Beads coated with dsDNA links were incubated with the well-characterized kinesin-1 construct K560 labeled with GFP (32) (Fig. 2 *a*). This construct contains a fragment of the kinesin-1 coiled-coil stalk and a short neck and consequently has a contour length of just ~24 nm. Taking into account SNAP-GBP (~2 nm), the total lengths of the short and long kinesin-1-dsDNA tethers were around 38 and 215 nm, respectively.

We then used laser tweezers to bring one such bead to a taxol-stabilized MT attached to a coverslip, as in a traditional bead motility assay (13) (Fig. 2 *b*; Video S3). With sparse motor coating, less than one-third of the beads walked (Fig. S4 *a*), implying that the beads were mostly driven by single-motor molecules (7,36). We recorded bead motions with 10 ms exposure and corrected the data for blurring, as described in Supporting Materials and Methods. Next, we generated two-dimensional bead position clouds, which revealed overall larger excursions of beads tethered via the long dsDNA link (Fig. 2, *c* and *d*). The MT-perpendicular components of these excursions were then compared with theoretical predictions. The model and experiment were highly consistent for the short tethers, but the experimental excursions for the long tether were slightly smaller than expected (Fig. 2, *e* and *f*).

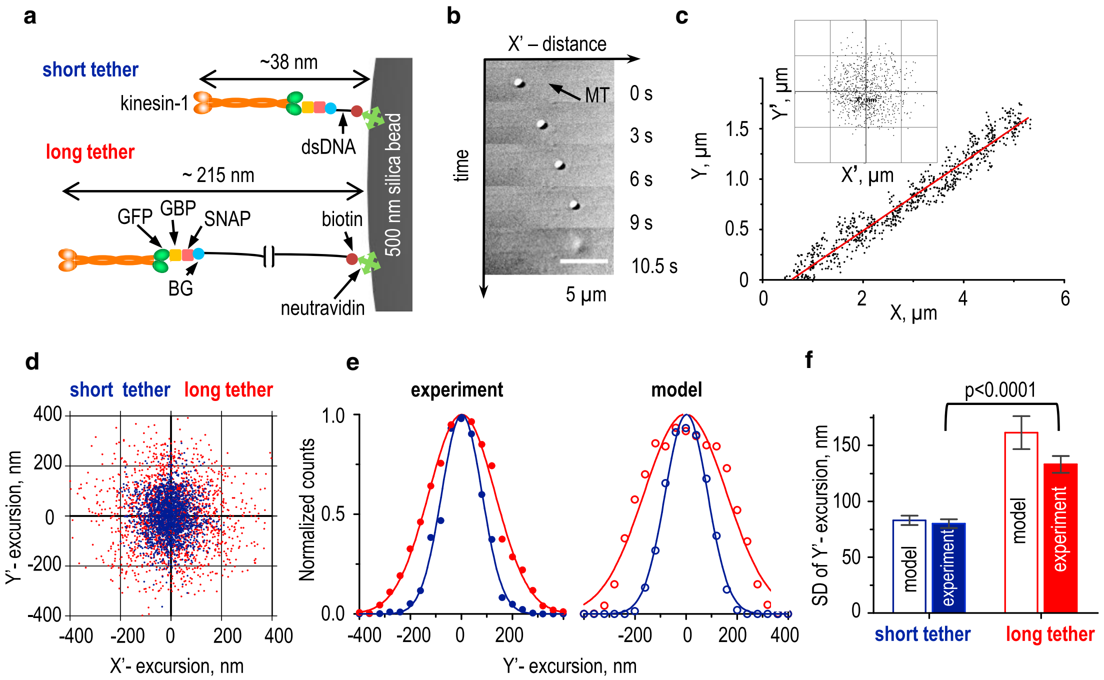

FIGURE 2 Verification of the TCM assay using kinesin-1 and dsDNA links. (*a*) Our strategy for conjugation of kinesin-1 to the surface of a glass bead via dsDNA links of different lengths. The SNAP-GBP protein adaptor enables connection of this GFP-labeled motor to the BG-labeled dsDNA. (*b*) Selected DIC images are shown of a bead transported by kinesin-1 linked via the long dsDNA link. The bead detached 10.5 s after the start of motion. (*c*) Experimental coordinates were collected for a bead conjugated to kinesin-1 via the long dsDNA link. The inset shows a cloud of excursions for this bead, calculated as the deviations of the bead's position from the line representing the MT (MT-perpendicular *Y'*-excursion) and from the assumed motor attachment site (MT-parallel *X'*-excursion); see Supporting Materials and Methods. The grid size is 0.2 μm. (*d*) Experimental cloud plots are shown for microbeads conjugated to kinesin-1 with different dsDNA links; representative data sets are based on the total 12,000 coordinates collected for 29 beads with the short tethers and 15,000 coordinates for 56 beads with the long tethers (for clarity, only 2000 randomly selected coordinates are shown for each tether). MT-parallel *X'*-excursions for these plots were calculated using the sliding averaging windows of 100–300 time points, corresponding to 1–3 s. (*e*) Normalized histograms show distributions of experimentally measured versus modeled bead *Y'*-excursions for the short (*blue*) and long (*red*) tethers. Each data set was fitted to a Gaussian function and normalized to its mean value. Each distribution is based on 2000 coordinates. (*f*) SDs of bead *Y'*-excursions are shown. Model predictions are based on data in Fig. 1 *e*. Experimental data were obtained from 29 beads with short tethers and 56 beads with long tethers. Error bars are SDs generated by bootstrap analysis; *p*-values were calculated by unpaired *t*-test. To see this figure in color, go online.

We hypothesized that, on average, lower-than-expected *Y'*-excursions could arise from stochastic variability in bead coating, leading to some of the beads having a high density of either dsDNA tethers or motors (Fig. 3 *a*). If several tethered motors are simultaneously engaged with the MT, bead excursions should be restricted (22). Higher dsDNA density could also reduce bead excursions if a single motor containing two GFPs binds two spatially separated dsDNA links, which is more likely to occur when the links are long. It is also conceivable that excessively high dsDNA density could create a dense, mechanically rigid layer around the bead, increasing its effective size and sterically reducing excursions, as illustrated with our theoretical model (Fig. S3, *c* and *d*). We tested these predictions by incubating beads with a high concentration of dsDNA (1 μM) and a limiting concentration of kinesin-1 (group 3, Fig. 3) or with a normal concentration of dsDNA (10 nM) and excess kinesin-1 (group 4, Fig. 3). Engagement of multiple kinesins did not change the bead's velocity, but it did increase the run length as expected (49), whereas denser dsDNA coating had no effect on these parameters (Fig. 3, *b* and *c*). In both cases, however, the MT-perpendicular bead excursions decreased by 10–20% (Fig. 3 *d*), explaining why the model, which used only one dsDNA-motor tether per bead, predicted slightly larger excursions. Importantly, these data show that the TCM method accurately discriminated the long and short tethers linking the walking motor and its microbead cargo.

Walking CENP-E kinesin forms a much shorter tether than predicted from its contour length

We then applied this method to examine the conformation of walking CENP-E kinesin. In FL CENP-E, the N-terminal motor domain is connected via a long stalk to the C-terminal tail, which contains a weak MT-binding site (Fig. S5 *a*) (12,13). This construct measures 230 ± 25 nm (12) in contour length, whereas the TR CENP-E construct is only ~10 nm long. These proteins were conjugated to beads via the C-terminal tags (Figs. 4 *a* and S5, *b* and *c*). Only a fraction of these beads moved, and their run lengths were consistent with a single-molecule regime (Fig. S5 *d*). Using

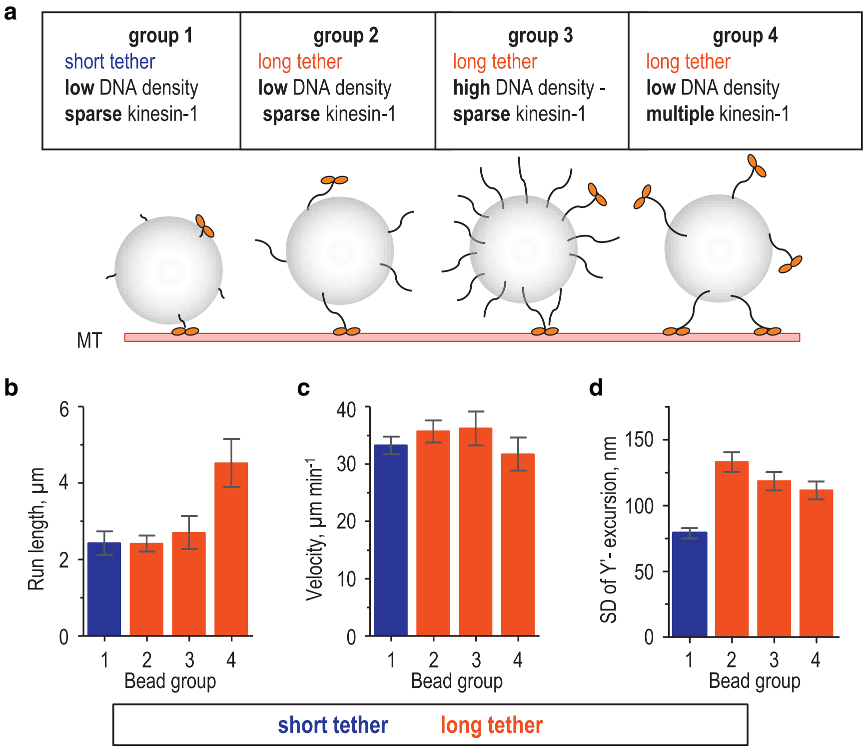

FIGURE 3 Impact of the high density of dsDNA links or motor molecules on bead excursions. (*a*) A diagram illustrates the four examined groups of kinesin-1 beads, which had different coatings. The length and density of dsDNA links and the density of kinesin-1 were varied to study the impact of these factors on bead excursions measured with the TCM assay. (*b* and *c*) Run length (*b*) and velocity (*c*) were measured for kinesin-1 beads; see (*a*). Data show the mean ± SEM measured at 30 μM Mg-ATP; $n = 29$, 40, 10, and 18 beads for groups 1, 2, 3, and 4, respectively. (*d*) Experimentally measured SD of Y'-excursions are shown based on $n = 29$, 56, 20, and 28 beads for groups 1, 2, 3, and 4, respectively. Error bars (SD) were generated by bootstrap analysis. To see this figure in color, go online.

the TCM assay, we observed the motility of beads driven by either of these motors, yielding clouds of bead excursions (Fig. 4 *b*) and distributions of the MT-perpendicular components (Fig. 4 *c*). Unexpectedly, these plots revealed only a slight difference between FL and TR CENP-E, suggesting that their effective tether lengths were similar. It seems unlikely that small excursions of the beads carried by FL CENP-E were caused by the nonspecific sticking of CENP-E stalk to bead surface because binding of this C-terminal GFP-labeled protein to the beads was through anti-GFP antibodies (Fig. S5 *c*; see Materials and Methods).

For TR CENP-E, the experimentally measured SD for MT-perpendicular bead excursions was 66 ± 4 nm, which is close to the theoretically predicted range for a 10 nm contour length (Fig. 4 *d*). Consistent with this, the TR CENP-E protein had slightly smaller MT-perpendicular excursions than those measured for the short dsDNA tether. By contrast, theoretical simulations for a bead carried via the 230 nm tether with $PL = 26$ nm, as in FL CENP-E, predicted the average end-to-end distance 125 ± 1 nm (mean ± SEM, $N = 2000$). Such a tether should generate bead excursions with the SD of $\sim$150 nm (Fig. 1 *e*). This is significantly larger than the experimentally measured SD of 70 ± 8 nm for FL CENP-E (Fig. 4 *d*), implying that despite its very large contour length, CENP-E kinesin forms a short tether with an average end-to-end distance of only $\sim$20 nm.

Sideways-pulling force cannot fully extend the stalk of a walking CENP-E kinesin

The simplest hypothesis to explain these relatively small bead excursions is that FL CENP-E is compacted, reducing the distance between the bead and the site of motor-domain attachment to the MT (Fig. 4 *e*, *top left panel*). However, CENP-E has a second MT-binding site located within the unstructured C-terminal tail (15), so the smaller-than-expected bead excursions may also reflect the short distance between the bead and the tail's MT attachment site (Fig. 4 *e*, *top right panel*). Previous measurements of the tail-MT binding interactions show that it is very transient, lasting $<$0.5 s, which is significantly shorter than the observation time during TCM assay. However, the estimated rebinding time for the tail and MT is even shorter ($<$1 ms (13)). Thus, during the TCM assay, the tail should be mostly MT-bound, and CENP-E with either compact or extended stalks would produce similarly small Brownian excursions.

We reasoned that we could discriminate whether the stalk is compact or extended by applying a sideways force on the bead carried by FL CENP-E because force should disrupt CENP-E tail binding to the MT (Fig. 4 *e*, *bottom row*). Indeed, even with no force, the tail dissociates from MT very frequently. Because its binding to MT is thermally driven, a small force pulling the tail away from the MT should prevent its rebinding, leaving the motor domains as the only MT attachment site. Moreover, a force acting on the MT-bound tail should also reduce its binding time

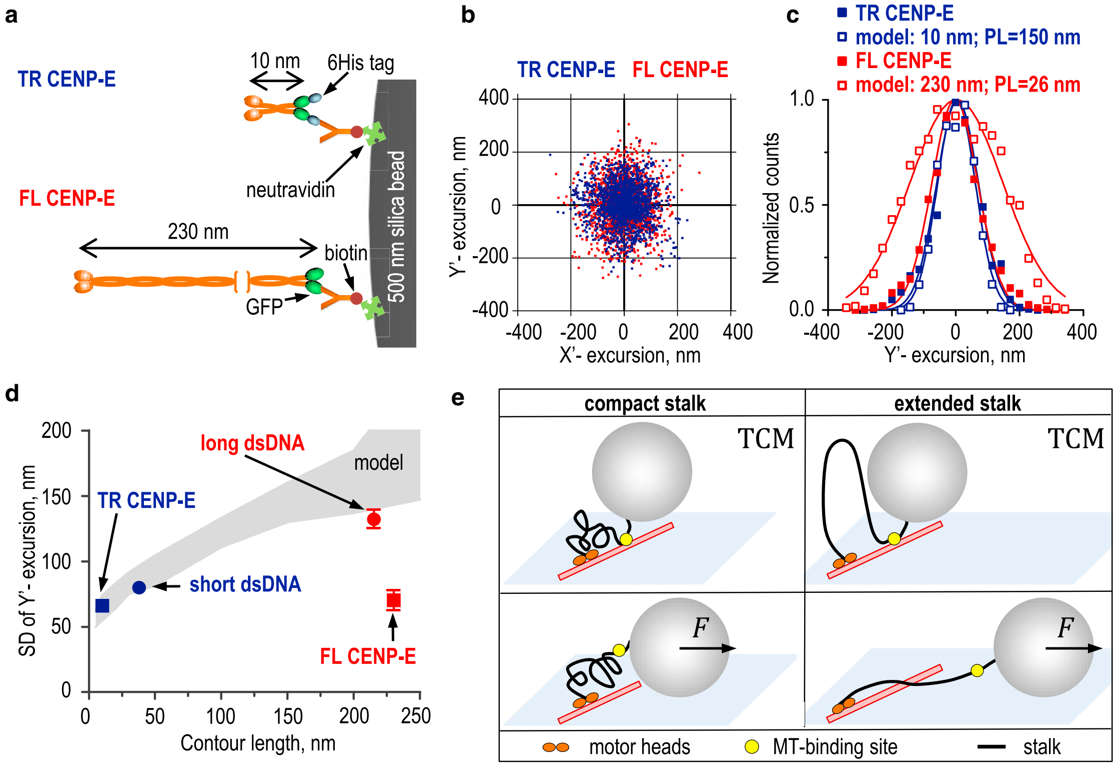

FIGURE 4 Analysis of bead excursions for wild-type (full-length (FL)) and truncated (TR) CENP-E kinesins. (*a*) A strategy is shown for conjugating CENP-E kinesins to microbead cargo. (*b*) Cloud plots show microbeads carried by different CENP-E kinesin constructs, based on 26 beads for TR CENP-E and 18 for FL CENP-E. For each tether, 2000 randomly selected coordinates are shown. (*c*) Histograms show distributions of experimentally measured (*solid symbols*) versus predicted MT-perpendicular (*Y'*) bead excursions (*open symbols*). CENP-E tethers were modeled with specified contour lengths and persistence lengths. Each distribution (based on 2000 coordinates) was fitted to a Gaussian function and normalized to its mean value. (*d*) SDs of bead *Y'*-excursions are shown versus the contour length of the molecular tether. Squares show experimental measurements for TR and FL CENP-E, and circles show experimental measurements for kinesin-1 with different dsDNA links. The gray area represents the theoretical prediction from Fig. 1 *e* for the range of PL = 26–150 nm, with 95% confidence. (*e*) Possible models show the FL CENP-E configuration to explain the low SD of the Brownian bead excursions. Upper cartoons show that if the MT-binding site (*yellow*) within the CENP-E tail is persistently attached to MT, in the TCM assay both compact and extended stalk configurations should lead to similarly small bead excursions limited only by the bead-proximal segment of the unstructured CENP-E tail. In lower cartoons, external sideways force prevents the tail's MT-binding and stretches CENP-E, limited by the compactness of the stalk (*left*). In the "extended" stalk model (*right*), the force-dependent bead displacement should increase up to the total contour length of CENP-E. To see this figure in color, go online.

(50). Using Bell's equation with a force-dependent transition step of 4 nm, we estimate that a 3 pN force should decrease the tail-MT binding time to 25 ms, and with 8 nm step this time would become only 1.3 ms. Thus, the applied force should dislodge the tail from MT, revealing the natural CENP-E length extension that is not obscured by the second MT binding site in its tail. If the CENP-E stalk is not compacted, the length of the bead-MT tether should increase up to 230 nm, which is much longer than measured from thermal motions in the TCM assay. If the CENP-E stalk is compacted, only a small bead displacement is predicted even in the presence of pulling force. Intermediate tether lengths could also be observed if the compact stalk can be partially extended by force.

To test these predictions, we designed an assay in which the motor-driven bead was pulled with a sideways force, applied by sweeping the optical trap perpendicular to the MT at a frequency of 1 Hz and an amplitude of 0.5 μm (Fig. 5 *a*; Video S4). The duration of one such cycle is significantly longer than the predicted attachment time of the CENP-E tail to MT under force. To facilitate the unambiguous identification of bead detachment events from the MT due to motor dissociation, we applied an additional small load (1 pN) to a moving bead with the force clamp, implemented via a feedback-controlled piezo stage (see Materials and Methods).

In Fig. 5 *b*, changes in the position of the bead (*top panel*) and stage (*bottom*) are plotted for one such experiment. Initially, the bead coated with FL CENP-E was brought close to the coverslip-immobilized MT, as in a regular TCM assay. After the CENP-E started walking (3.7 s), the sideways-trap sweeping and force clamp were triggered. Consequently, the MT-perpendicular bead coordinate started to change periodically (*green curve* in the *top panel*). The bead continued to move along the MT during the first two cycles of sideways sweeping, as seen from the

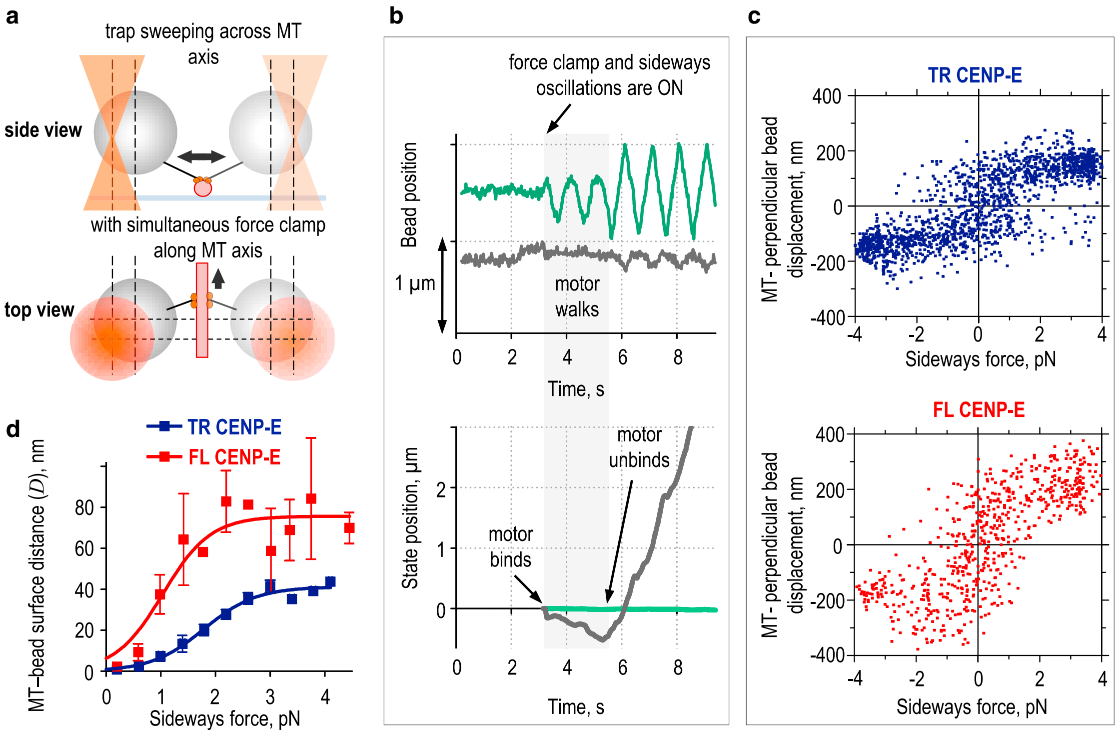

FIGURE 5 Probing CENP-E conformation with a sideways force. (*a*) Schematics show the sideways-force experiment from two different views. The MT cylinder (in *red*) is attached to the coverslip (*blue*), shown only from a side view (*top image*). A bead tethered to the MT-bound motor (*small circles*) is shown in two extreme positions, corresponding to the amplitude of sideways motion (*double-headed arrow*). The laser trap, also shown in two extreme positions, is depicted by triangles in the side view and large orange circles in the top view. The bead's displacement from the trap's center (*broken lines*) indicates the presence of the sideways force and the force clamp opposing the motor's motion along the MT. The arrow in the top view shows the direction of motor walking. (*b*) An example experiment with the sideways force is shown. The upper graph shows displacement of the bead in the direction across (*green*) and along (*gray*) the MT; for clarity, the curves are offset vertically. The bottom graph shows displacements of the piezo stage in the same experiment. The piezo stage starts moving after the force clamp is engaged, indicating that kinesin is walking along the MT. The amplitude of sideways bead displacement (*green curve* in *upper* graph) increases up to 1 μm after the motor unbinds from the MT and the bead is no longer tethered to the MT. (*c*) MT-perpendicular bead displacements under the sideways force are shown, calculated with Eq. 1 for beads carried by TR CENP-E, n = 17, and for FL CENP-E, n = 9. (*d*) The mean distance *D* between the MT and bead surface is shown as a function of the sideways force, calculated based on the data in (*c*) and Fig. S5 *e*, using Eq. 2 in Materials and Methods. Solid lines are fits to sigmoid functions, and bars are SEMs. To see this figure in color, go online.

continuous motion of the stage along the MT axis (*gray curve* in the *bottom panel*). When CENP-E unbound from the MT (~6 s), the direction and velocity of stage motion changed abruptly, as the stage tried to maintain the clamped force on the freed bead. Importantly, the top panel shows that the sideways displacement of the bead under force was relatively small during motor walking, indicating that bead displacement was restricted by the tether. After the bead detached, however, its sideways motion was no longer restricted, and the bead's position mirrored the trajectory of optical trap, exhibiting a full 1 μm amplitude (*top panel*, *green curve*).

We used this assay with CENP-E-coated beads to extract bead displacement in the MT-perpendicular direction as a function of the applied sideways force (Fig. 5 *c*). Taking into account the bead's diameter (Fig. S5 *e*), we calculated the distance from the bead surface to the MT and plotted these binned data as a function of the sideways force (Fig. 5 *d*). This distance increased with applied sideways force for beads coated with either TR or FL CENP-E. For a TR motor, it reached a plateau of 41 ± 1 nm. This maximal deviation exceeds the total estimated contour length for TR CENP-E, indicating the presence of some additional compliant element. The compliance is likely to result from the slight looping (bending or twisting) of the MT from the sites of coverslip attachment (via antitubulin antibodies) under the sideways force. However, because the MTs were attached to the coverslips using the same antibody concentration in all experiments, such MT looping should be the same for both TR and FL CENP-E. Thus, the offset between the plateau values for the TR and FL CENP-E curves in Fig. 5 *d* (35 ± 4 nm) corresponds to the difference in the maximal extension lengths of these two proteins. Because the contour length of TR CENP-E does not exceed 10 nm, these data show that FL CENP-E can be extended up to ~45 nm under sideways force. This is ~2-fold longer than the average tether length deduced from the TCM assay, suggesting partial FL CENP-E extension under 3–4 pN force. Importantly, the sideways force failed to extend the CENP-E molecule completely, strongly

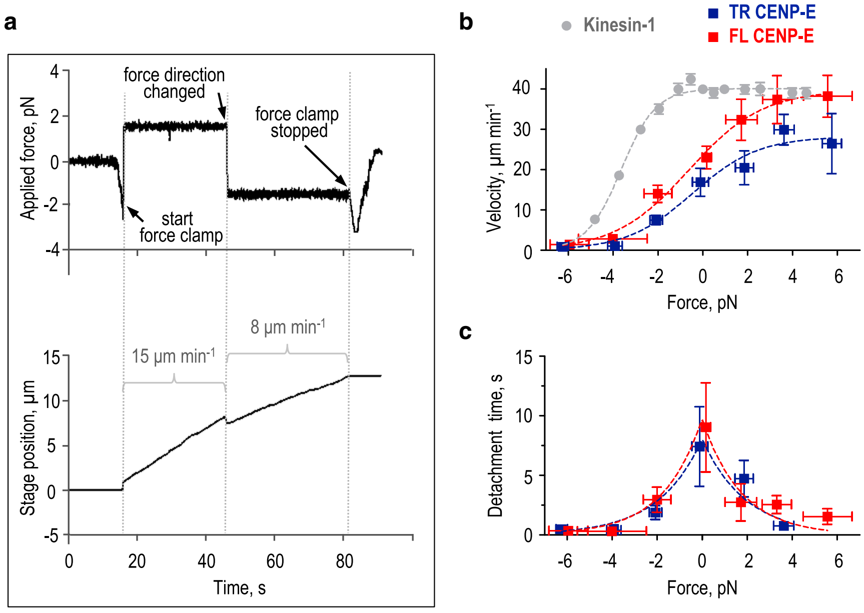

FIGURE 6 Measurement of the response of CENP-E kinesin to mechanical load. (*a*) An example experiment is shown in which a CENP-E-coated bead moves under the assisting force (2 pN) and then the opposing force (−2 pN), acting along the MT. The upper panel shows the force applied to the bead, and the lower panel shows the motion of the stage, which was programmed to keep a constant distance between the centers of the bead and optical trap. (*b*) Force-velocity curves show TR and FL CENP-E in comparison with the published data for kinesin-1 (*gray* (51)). Assisting load is indicated by positive numbers, and opposing force is indicated by negative numbers. Symbols show mean ± SEM based on at least 60 measurements for each CENP-E motor. The lines represent fits to Eq. 3; see Materials and Methods. (*c*) Force-dependent detachment time for TR and FL CENP-E motors is shown. Lines represent fits to Eq. 4; see Materials and Methods and the legend to (*b*) for other details. To see this figure in color, go online.

suggesting that walking FL CENP-E kinesin has a compact configuration.

The compact configuration of FL CENP-E does not impede its transport function

Because walking FL CENP-E kinesin does not behave as an elongated fibrillar tether, we next investigated whether its compact configuration interferes with load-bearing. To test the range of directional loads, we used an optical force clamp along the MT in the absence of the sideways force, as illustrated by recordings from a typical experiment in Fig. 6 *a*. TR CENP-E, which was used as a control, slowed down significantly under the opposing load and eventually stalled at −4.4 ± 0.8 pN, a slightly smaller stall force than reported previously for artificially dimerized CENP-E motor heads (37). The FL CENP-E kinesin stalled at a similar load of −4.6 ± 0.3 pN (Fig. 6 *b*). Assisting forces up to 6 pN increased the velocity of TR CENP-E transport by ~70%. Analogous measurements using beads coated with FL CENP-E revealed that under the assisting load, this motor walked noticeably faster; under the 5–6 pN load, FL CENP-E walked at 38 ± 5 μm min^{-1}, whereas the velocity of TR CENP-E was 26 ± 7 μm min^{-1} (Fig. 6 *b*). This is in contrast to conventional kinesin-1, which does not accelerate significantly under assisting force (51).

To compare the force-velocity dependencies of the FL and TR CENP-E motors in a more rigorous manner, we fit them with the previously proposed energy-landscape model (42) (see Materials and Methods). Although FL and TR CENP-E had similar fractions of biochemical transitions ($p_{TR} = 0.58 \pm 0.10$ vs. $p_{FL} = 0.59 \pm 0.05$), their unloaded catalytic rates were different ($k_{o,TR} = 33.3 \pm 3.3$ vs. $k_{o,FL} = 48.3 \pm 1.6$ s^{-1}), which was consistent with a slightly faster velocity of FL CENP-E molecules with no load (13). The characteristic distances associated with the force-dependence of these two constructs were comparable ($\delta_{TR} = 2.8 \pm 0.8$ nm vs. $\delta_{FL} = 2.5 \pm 0.3$ nm), implying that the compact configuration did not significantly alter the response of CENP-E to force. Moreover, with the applied force, the run times decreased similarly for both proteins (Fig. 6 *c*). Exponential fitting of these dependencies using Eq. 4 in Materials and Methods yielded very similar values for the detachment force: 1.9 ± 0.5 pN for TR vs. 1.7 ± 0.3 pN for FL CENP- E. Thus, the compact configuration of the CENP-E motor limits the range of cargo motion without strongly influencing the ability of the motor to walk under assisting or opposing forces.

DISCUSSION

The predicted structures of nonmotor regions differ dramatically among members of the kinesin superfamily, but little is known about the resultant mechanical properties of cargo tethering in transporting kinesins. The dynamic configurations of stalk- and tail-mediated tethers may affect the ability of motors to move collectively and/or to navigate through complex cytoplasmic environments (29,52–54). Potentially, these tethers can also tune the reach from motor-bound cargo to cytoskeletal tracks or serve as tension-sensitive elements to control the motor's function or conformation in response to load. To begin addressing these issues, we combined experiments and theory to develop the TCM assay. This method is applicable to tethers formed by kinesin nonmotor domains, as we demonstrated for CENP-E (Fig. 4 *a*), or to tethers engineered using heterologous fibrillar links, such as dsDNA (Fig. 2 *a*). To our knowledge, our work provides the first experimental and theoretical guide for probing the mechanical properties of motor-bead tethering that takes into account uncertainties arising due to variability of motor velocity and the presence of multiple protofilament tracks. The major advantage of the TCM assay over traditional TPM and tethered fluorophore motion approaches is that it affords a straightforward identification of single, actively walking molecules. Purified kinesins often display heterogeneous behavior; for example, in in vitro preparations of FL CENP-E, only a fraction of motors exhibit directed motility, whereas other molecules fail to bind to MTs (presumably because of autoinhibitory folding (55)) and others bind very transiently or exhibit diffusive motions (13). TCM naturally selects only the motile molecules and consequently reports on the conformation of transporting motors free of intramolecular interactions that modify their activity.

The TCM approach provides important insights into the dynamic configuration of one of the longest kinesin family members, CENP-E. Early in mitosis, this kinesin binds to the kinetochore via a site upstream of the MT-binding site in its C-terminal tail (Fig. S6 *a*). In the absence of MTs, the kinetochore-bound CENP-E is likely to be fully elongated, contributing to the appearance of a dense and fibrillar kinetochore "corona" (56). This extension is beneficial early in mitosis because it expands the range of MT search and capture by the heads of CENP-E motors tethered to the kinetochore (12). However, the results of this in vitro study reveal that the stalk of CENP-E engaged in active transport along the MT wall does not behave as an elongated fibrillar tether, arguing against the idea that CENP-E is fully extended at the MT-bound kinetochores. Using a laser trap, we applied a 3–4 pN force on a bead attached to the C-terminus of the walking CENP-E, but the tether could not be extended more than twofold (Fig. 5 *d*). The force pulling on the bead should disrupt binding between the MT and the C-terminal tail of CENP-E, revealing its natural extension length (Fig. 4 *e*). Thus, the lack of significant elongation of CENP-E under the sideways force suggests that the stalk of the walking CENP-E is compacted. The estimated end-to-end length of transporting CENP-E in vitro is only 20 nm, which is $<10\%$ of its contour length and $\sim 16\%$ of its predicted end-to-end length. In contrast, the tether formed by the K560 kinesin-1 fragment, as measured using a heterologous dsDNA linker, is $\sim 80\%$ of its contour length, so our finding is specific to CENP-E.

Our conclusion that CENP-E transports in a compact configuration is consistent with the reduced length estimated for kinetochore-bound CENP-E from high-resolution mapping of human kinetochore (57). Importantly, our experiments with laser tweezers argue against the model in which this compact configuration modifies load-bearing by CENP-E. The stall force of FL CENP-E is very similar to that of the CENP-E with no stalk, and both motors increase their velocity to similar degrees under the assisting force. This acceleration and the small detachment force (~ 1.8 pN) are in contrast to those of kinesin-1 (Fig. 6 *b*), which has an almost 1.7-fold greater detachment force (43). Previously, we showed that unlike kinesin-1, CENP-E responds to the opposing load with only a mild increase in backward stepping (40). Together with the findings reported here, these observations imply important differences in the transport functions of these two motor families. The specific force-velocity and detachment characteristics of CENP-E are likely to be responsible for its distinctive collective behavior (58) during chromosome transport, which is an important topic for future investigation.

In summary, our findings using the TCM assay and laser tweezers strongly suggest that the compact CENP-E configuration is regulatory rather than mechanical in nature. Because shortening of the CENP-E stalk leads to severe defects in chromosome segregation (16), the dynamic changes in CENP-E configuration appear to be essential for some function of CENP-E unrelated to transport. The noninhibitory CENP-E folding upon MT capture could serve to ensure that by reaching the MT plus-end, CENP-E motor domains facilitate close encounters between the MT tip and other kinetochore proteins (Fig. S6 *b*). Direct contact between MT tips and the kinetochore-associated MT-binding proteins is essential for the establishment and maintenance of the MT end-on configuration, and these contacts would be less likely if CENP-E molecules were fully extended. In this respect, it is revealing that CENP-E binds numerous kinetochore and MT regulators, including Mad1, PP1, CENP-F, CLASPs, and SKAP (59–63). At the dynamic MT tip, the folded CENP-E stalk could provide a mobile molecular platform to bind and translocate these important regulators. Given that the compact CENP-E stalk can be partially extended by force, the association of these regulators with CENP-E could be regulated by tension between the MT-bound CENP-E motor domain and its kinetochore-binding domain (Fig. S6 *b*). Whether CENP-E helps to localize various kinetochore regulators in a tension-sensitive manner at the kinetochore-embedded MT ends is an interesting question for future cell biological studies.

SUPPORTING MATERIAL

Supporting Materials and Methods, six figures, one table, and four videos are available at http://www.biophysj.org/biophysj/supplemental/S0006-3495(18)30463-6.

AUTHOR CONTRIBUTIONS

N.G., E.V.T., F.I.A., and E.L.G. designed the study. N.G. and E.V.T. performed the experiments and analyzed the data. N.G., V.M., and F.I.A. carried out the theoretical analyses. B.V. and D.W.C. contributed an essential reagent. A.L.D. developed the protocol for dsDNA-bead conjugation. N.G., E.V.T., and E.L.G. wrote the manuscript with input from V.M. and F.I.A.

ACKNOWLEDGMENTS

We thank Y. Kim, V. Korneeva, E. Santana, P. Zakharov, and A. Kiyatkin for assistance with protein purification; A. Sabantsev for assistance with developing the TCM assay; A. Zaytsev for technical assistance; J.R. McIntosh for help at the initial stages of this project; and M. Ostap and members of the Grishchuk and Ataullakhanov laboratories for stimulating discussions.

This work was supported in part by grants from the National Institutes of Health to E.L.G. (R01-GM098389) and from the Russian Foundation for Basic Research (16-04-00390 A, 13-04-40188-H, and 13-04-40190-H to F.I.A. and 14-04-31961 to N.G.). Theoretical modeling was supported by grant 16-14-00-224 from the Russian Science Foundation to F.I.A. E.L.G. was supported in part by research scholar grant RSG-14-018-01-CCG from the American Cancer Society. B.V. was supported by a postdoctoral fellowship from the Human Frontiers Science Program Long-Term Fellowship (LT000855/2010). D.W.C. received salary support from the Ludwig Institute for Cancer Research.

SUPPORTING CITATIONS

References (64,65) appear in the Supporting Material.

REFERENCES

1. Verhey, K. J., and J. W. Hammond. 2009. Traffic control: regulation of kinesin motors. *Nat. Rev. Mol. Cell Biol.* 10:765–777.
2. Hirokawa, N., S. Niwa, and Y. Tanaka. 2010. Molecular motors in neurons: transport mechanisms and roles in brain function, development, and disease. *Neuron.* 68:610–638.
3. van Riel, W. E., A. Rai, …, A. Akhmanova. 2017. Kinesin-4 KIF21B is a potent microtubule pausing factor. *eLife.* 6:e24746.
4. Mayr, M. I., M. Storch, …, T. U. Mayer. 2011. A non-motor microtubule binding site is essential for the high processivity and mitotic function of kinesin-8 Kif18A. *PLoS One.* 6:e27471.
5. Hirokawa, N., K. K. Pfister, …, G. S. Bloom. 1989. Submolecular domains of bovine brain kinesin identified by electron microscopy and monoclonal antibody decoration. *Cell.* 56:867–878.
6. Kerssemakers, J., J. Howard, …, S. Diez. 2006. The distance that kinesin-1 holds its cargo from the microtubule surface measured by fluorescence interference contrast microscopy. *Proc. Natl. Acad. Sci. USA.* 103:15812–15817.
7. Li, Q., S. J. King, …, J. Xu. 2016. Quantitative determination of the probability of multiple-motor transport in bead-based assays. *Biophys. J.* 110:2720–2728.
8. Jeney, S., E. H. Stelzer, …, E. L. Florin. 2004. Mechanical properties of single motor molecules studied by three-dimensional thermal force probing in optical tweezers. *Chemphyschem.* 5:1150–1158.
9. Putkey, F. R., T. Cramer, …, D. W. Cleveland. 2002. Unstable kinetochore-microtubule capture and chromosomal instability following deletion of CENP-E. *Dev. Cell.* 3:351–365.
10. Zasadil, L. M., E. M. Britigan, …, B. A. Weaver. 2016. High rates of chromosome missegregation suppress tumor progression but do not inhibit tumor initiation. *Mol. Biol. Cell.* 27:1981–1989.
11. Liang, M. L., T. H. Hsieh, …, H. W. Wang. 2016. Downregulation of miR-137 and miR-6500-3p promotes cell proliferation in pediatric high-grade gliomas. *Oncotarget.* 7:19723–19737.
12. Kim, Y., J. E. Heuser, …, D. W. Cleveland. 2008. CENP-E combines a slow, processive motor and a flexible coiled coil to produce an essential motile kinetochore tether. *J. Cell Biol.* 181:411–419.
13. Gudimchuk, N., B. Vitre, …, E. L. Grishchuk. 2013. Kinetochore kinesin CENP-E is a processive bi-directional tracker of dynamic microtubule tips. *Nat. Cell Biol.* 15:1079–1088.
14. Seeger, M. A., Y. Zhang, and S. E. Rice. 2012. Kinesin tail domains are intrinsically disordered. *Proteins.* 80:2437–2446.
15. Liao, H., G. Li, and T. J. Yen. 1994. Mitotic regulation of microtubule cross-linking activity of CENP-E kinetochore protein. *Science.* 265:394–398.
16. Vitre, B., N. Gudimchuk, …, E. L. Grishchuk. 2014. Kinetochore-microtubule attachment throughout mitosis potentiated by the elongated stalk of the kinetochore kinesin CENP-E. *Mol. Biol. Cell.* 25:2272–2281.
17. Gelles, J., B. J. Schnapp, and M. P. Sheetz. 1988. Tracking kinesin-driven movements with nanometre-scale precision. *Nature.* 331:450–453.
18. Wang, Z., S. Khan, and M. P. Sheetz. 1995. Single cytoplasmic dynein molecule movements: characterization and comparison with kinesin. *Biophys. J.* 69:2011–2023.
19. Brinkers, S., H. R. Dietrich, …, B. Rieger. 2009. The persistence length of double stranded DNA determined using dark field tethered particle motion. *J. Chem. Phys.* 130:215105.
20. Han, L., B. Lui, …, R. Phillips. 2009. Calibration of tethered particle motion experiments. *In* Mathematics of DNA Structure, Function and Interactions. C. J. Benham, S. Harvey, W. K. Olson, D. W. Sumners, and D. Swigon, eds. Springer, pp. 123–138.
21. Nelson, P. C., C. Zurla, …, D. Dunlap. 2006. Tethered particle motion as a diagnostic of DNA tether length. *J. Phys. Chem. B.* 110:17260–17267.
22. Pouget, N., C. Dennis, …, L. Salomé. 2004. Single-particle tracking for DNA tether length monitoring. *Nucleic Acids Res.* 32:e73.
23. Towles, K. B., J. F. Beausang, …, P. C. Nelson. 2009. First-principles calculation of DNA looping in tethered particle experiments. *Phys. Biol.* 6:025001.
24. Dohoney, K. M., and J. Gelles. 2001. Chi-sequence recognition and DNA translocation by single RecBCD helicase/nuclease molecules. *Nature.* 409:370–374.
25. Yin, H., R. Landick, and J. Gelles. 1994. Tethered particle motion method for studying transcript elongation by a single RNA polymerase molecule. *Biophys. J.* 67:2468–2478.
26. Merkus, K. E., M. W. J. Prins, and C. Storm. 2016. Single-bond association kinetics determined by tethered particle motion: concept and simulations. *Biophys. J.* 111:1612–1620.
27. Schafer, D. A., J. Gelles, …, R. Landick. 1991. Transcription by single molecules of RNA polymerase observed by light microscopy. *Nature.* 352:444–448.
28. May, P. F. J., J. N. M. Pinkney, …, A. N. Kapanidis. 2014. Tethered fluorophore motion: studying large DNA conformational changes by single-fluorophore imaging. *Biophys. J.* 107:1205–1216.
29. Michalek, A. J., G. G. Kennedy, …, M. Y. Ali. 2015. Flexural stiffness of Myosin Va subdomains as measured from tethered particle motion. *J. Biophys.* 2015:465693.
30. Miller, H. P., and L. Wilson. 2010. Preparation of microtubule protein and purified tubulin from bovine brain by cycles of assembly and disassembly and phosphocellulose chromatography. *Methods Cell Biol.* 95:3–15.
31. Hyman, A., D. Drechsel, …, T. Mitchison. 1991. Preparation of modified tubulins. *Methods Enzymol.* 196:478–485.
32. Case, R. B., D. W. Pierce, …, R. D. Vale. 1997. The directional preference of kinesin motors is specified by an element outside of the motor catalytic domain. *Cell.* 90:959–966.
33. Kubala, M. H., O. Kovtun, …, B. M. Collins. 2010. Structural and thermodynamic analysis of the GFP:GFP-nanobody complex. *Protein Sci.* 19:2389–2401.
34. Qiu, W., N. D. Derr, …, S. L. Reck-Peterson. 2012. Dynein achieves processive motion using both stochastic and coordinated stepping. *Nat. Struct. Mol. Biol.* 19:193–200.

35. Grishchuk, E. L., I. S. Spiridonov, …, J. R. McIntosh. 2008. Different assemblies of the DAM1 complex follow shortening microtubules by distinct mechanisms. *Proc. Natl. Acad. Sci. USA.* 105:6918–6923.

36. Svoboda, K., and S. M. Block. 1994. Force and velocity measured for single kinesin molecules. *Cell.* 77:773–784.

37. Yardimci, H., M. van Duffelen, …, P. R. Selvin. 2008. The mitotic kinesin CENP-E is a processive transport motor. *Proc. Natl. Acad. Sci. USA.* 105:6016–6021.

38. Volkov, V. A., A. V. Zaytsev, and E. L. Grishchuk. 2014. Preparation of segmented microtubules to study motions driven by the disassembling microtubule ends. *J. Vis. Exp.* 85:e51150.

39. Grishchuk, E. L., A. K. Efremov, …, F. I. Ataullakhanov. 2008. The Dam1 ring binds microtubules strongly enough to be a processive as well as energy-efficient coupler for chromosome motion. *Proc. Natl. Acad. Sci. USA.* 105:15423–15428.

40. Barisic, M., R. Silva e Sousa, …, H. Maiato. 2015. Mitosis. Microtubule detyrosination guides chromosomes during mitosis. *Science.* 348:799–803.

41. Simmons, R. M., J. T. Finer, …, J. A. Spudich. 1996. Quantitative measurements of force and displacement using an optical trap. *Biophys. J.* 70:1813–1822.

42. Schnitzer, M. J., K. Visscher, and S. M. Block. 2000. Force production by single kinesin motors. *Nat. Cell Biol.* 2:718–723.

43. Müller, M. J., S. Klumpp, and R. Lipowsky. 2008. Tug-of-war as a cooperative mechanism for bidirectional cargo transport by molecular motors. *Proc. Natl. Acad. Sci. USA.* 105:4609–4614.

44. Wang, M. D., H. Yin, …, S. M. Block. 1997. Stretching DNA with optical tweezers. *Biophys. J.* 72:1335–1346.

45. Wolgemuth, C. W., and S. X. Sun. 2006. Elasticity of alpha-helical coiled coils. *Phys. Rev. Lett.* 97:248101.

46. Segall, D. E., P. C. Nelson, and R. Phillips. 2006. Volume-exclusion effects in tethered-particle experiments: bead size matters. *Phys. Rev. Lett.* 96:088306.

47. Juillerat, A., T. Gronemeyer, …, K. Johnsson. 2003. Directed evolution of O6-alkylguanine-DNA alkyltransferase for efficient labeling of fusion proteins with small molecules in vivo. *Chem. Biol.* 10:313–317.

48. Rothbauer, U., K. Zolghadr, …, H. Leonhardt. 2006. Targeting and tracing antigens in live cells with fluorescent nanobodies. *Nat. Methods.* 3:887–889.

49. Xu, J., Z. Shu, …, S. P. Gross. 2012. Tuning multiple motor travel via single motor velocity. *Traffic.* 13:1198–1205.

50. Gergely, C., J. Voegel, …, J. Hemmerlé. 2000. Unbinding process of adsorbed proteins under external stress studied by atomic force microscopy spectroscopy. *Proc. Natl. Acad. Sci. USA.* 97:10802–10807.

51. Block, S. M., C. L. Asbury, …, M. J. Lang. 2003. Probing the kinesin reaction cycle with a 2D optical force clamp. *Proc. Natl. Acad. Sci. USA.* 100:2351–2356.

52. Brunnbauer, M., R. Dombi, …, Z. Ökten. 2012. Torque generation of kinesin motors is governed by the stability of the neck domain. *Mol. Cell.* 46:147–158.

53. Bruno, L., M. Salierno, …, V. Levi. 2011. Mechanical properties of organelles driven by microtubule-dependent molecular motors in living cells. *PLoS One.* 6:e18332.

54. Bieling, P., I. A. Telley, …, T. Surrey. 2008. Processive kinesins require loose mechanical coupling for efficient collective motility. *EMBO Rep.* 9:1121–1127.

55. Espeut, J., A. Gaussen, …, A. Abrieu. 2008. Phosphorylation relieves autoinhibition of the kinetochore motor Cenp-E. *Mol. Cell.* 29:637–643.

56. Cooke, C. A., B. Schaar, …, W. C. Earnshaw. 1997. Localization of CENP-E in the fibrous corona and outer plate of mammalian kinetochores from prometaphase through anaphase. *Chromosoma.* 106:446–455.

57. Wan, X., R. P. O'Quinn, …, E. D. Salmon. 2009. Protein architecture of the human kinetochore microtubule attachment site. *Cell.* 137:672–684.

58. Arpag, G., S. Shastry, …, E. Tuzel. 2014. Transport by populations of fast and slow kinesins uncovers novel family-dependent motor characteristics important for in vivo function. *Biophys. J.* 107:1896–1904.

59. Akera, T., Y. Goto, …, Y. Watanabe. 2015. Mad1 promotes chromosome congression by anchoring a kinesin motor to the kinetochore. *Nat. Cell Biol.* 17:1124–1133.

60. Chan, G. K., B. T. Schaar, and T. J. Yen. 1998. Characterization of the kinetochore binding domain of CENP-E reveals interactions with the kinetochore proteins CENP-F and hBUBR1. *J. Cell Biol.* 143:49–63.

61. Huang, Y., W. Wang, …, X. Yao. 2012. CENP-E kinesin interacts with SKAP protein to orchestrate accurate chromosome segregation in mitosis. *J. Biol. Chem.* 287:1500–1509.

62. Kim, Y., A. J. Holland, …, D. W. Cleveland. 2010. Aurora kinases and protein phosphatase 1 mediate chromosome congression through regulation of CENP-E. *Cell.* 142:444–455.

63. Maffini, S., A. R. Maia, …, H. Maiato. 2009. Motor-independent targeting of CLASPs to kinetochores by CENP-E promotes microtubule turnover and poleward flux. *Curr. Biol.* 19:1566–1572.

64. Lupas, A., M. Van Dyke, and J. Stock. 1991. Predicting coiled coils from protein sequences. *Science.* 252:1162–1164.

65. Alberts, B., A. Johnson, …, T. Hunt. 2015. Ch3. Proteins: the shape and structure of proteins. Molecular Biology of the Cell, Sixth edition. Garland Science, Taylor and Francis Group, p. 116.

Biophysical Journal, Volume *114*

Supplemental Information

Probing Mitotic CENP-E Kinesin with the Tethered Cargo Motion Assay and Laser Tweezers

Nikita Gudimchuk, Ekaterina V. Tarasovetc, Vadim Mustyatsa, Alexei L. Drobyshev, Benjamin Vitre, Don W. Cleveland, Fazly I. Ataullakhanov, and Ekaterina L. Grishchuk

Supporting Materials and Methods

Supporting Methods

Experimental procedures

dsDNA sequences. Short dsDNA links were produced using the following primers: (1) biotin-5′-CCT ATC TCG GTC TAT TCT TTT GAT TTA TAA GGG A-3′ and (2) BG-5′-TCC CTT ATA AAT CAA AAG AAT AGA CCG AGA TAG G-3′. Long dsDNA links were prepared using PCR primer (1), as above, and (3) BG-5′-ACC AAG TCA TTC TGA GAA TAG TGT ATG C-3′. The resulting dsDNA sequence for a short link was: biotin-CCT ATC TCG GTC TAT TCT TTT GAT TTA TAA GGG A-BG. Sequence of the long link: biotin-CCT ATC TCG GTC TAT TCT TTT GAT TTA TAA GGG ATT TTG CCG ATT TCG GCC TAT TGG TTA AAA AAT GAG CTG ATT TAA CAA AAA TTT AAC GCG AAT TTT AAC AAA ATA TTA ACG TTT ACA ATT TCA GGT GGC ACT TTT CGG GGA AAT GTG CGC GGA ACC CCT ATT TGT TTA TTT TTC TAA ATA CAT TCA AAT ATG TAT CCG CTC ATG AGA CAA TAA CCC TGA TAA ATG CTT CAA TAA TAT TGA AAA AGG AAG AGT ATG AGT ATT CAA CAT TTC CGT GTC GCC CTT ATT CCC TTT TTT GCG GCA TTT TGC CTT CCT GTT TTT GCT CAC CCA GAA ACG CTG GTG AAA GTA AAA GAT GCT GAA GAT CAG TTG GGT GCA CGA GTG GGT TAC ATC GAA CTG GAT CTC AAC AGC GGT AAG ATC CTT GAG AGT TTT CGC CCC GAA GAA CGT TTT CCA ATG ATG AGC ACT TTT AAA GTT CTG CTA TGT GGC GCG GTA TTA TCC CGT ATT GAC GCC GGG CAA GAG CAA CTC GGT CGC CGC ATA CAC TAT TCT CAG AAT GAC TTG GT-BG.

Additional methods for data analyses

Estimation of the correction factor to compensate for image blurring. In the TCM assay, the CCD camera exposure time for collecting one bead image was 10 ms. During this exposure time, a bead moves continuously due to Brownian motion, and its image becomes slightly blurred, potentially leading to an underestimation of the measured SD. We assessed the extent of this underestimation in our experimental conditions by measuring the SD for Brownian fluctuations of 0.5 μm glass beads held in a laser trap with known stiffness (Fig. S4c). Bead motion was recorded simultaneously with a CCD camera and QPD, which collects bead positions at 100 kHz (10 μs); consequently, the underestimation by QPD is negligible. By extrapolating the ratio of the SDs estimated based on the camera and QPD measurements to zero trapping stiffness, we found that the underestimation in camera recording of an untrapped bead was about 0.7 (Fig. S4d). Because the slope of this dependency is small, potential differences in the blurring effect for tethers with SD of excursions in our experimental range (60-130 nm) were not considered, and the same correction factor was applied to all measurements. Thus, the experimentally determined SDs for bead excursions in the TCM assay were divided by this factor, and these adjusted SD values were compared with model predictions, which are free from blurring.

Plotting the bead clouds. To plot the coordinates of the bead's center in two dimensions (cloud plots), we first calculated the MT-perpendicular bead excursions (Y'-excursions), as described in "Analysis of experimental TCM data" in Materials and Methods. However, the MT-parallel bead excursions (X'-excursions) from the MT-attached motor domains are not known with certainty because the exact position of the motor heads at each time point is unknown. One approach to this problem is to estimate position of the motor from the averaged (smoothed) bead trajectory. This approach seems reasonable because the motor moves much slower than the Brownian motion of the bead (kHz frequency with 50–150 nm amplitude). Thus, for each motor position on the MT, the bead visits many points of the available space. Assuming that the mean bead excursion is close to zero in the moving coordinate system, the position of the motor on the MT in this system can be approximated by the averaged bead positions, such as obtained by smoothing the bead trajectory. By subtracting this estimated position of the motor domain from the individual X’ coordinates of the center of the bead, one can obtain X’-excursions and plot bead clouds. Using this approach, we constructed cloud plots for one representative experiment with a long tether. To examine validity of this approach we used different sliding averaging windows: with 5–250 time points, corresponding to 50–2,500 ms. Three representative plots are shown in Fig. S4e. Clearly, the shape of the cloud in the MT-parallel (X’) direction depends on the size of the averaging window. For smoothing sliding windows with larger N, the difference between the smoothed and non-smoothed coordinates is larger, so with increasing N the cloud expands in the MT-parallel direction. Thus, unlike in the traditional TPM assay in which the tether’s attachment point is fixed, cloud plots for a motor-transported bead cannot be used for quantitative analysis and we present that only for illustration (Figs. 2d and 4b). Because determining the MT-perpendicular excursions does not involve trajectory smoothing and is free from this artefact, our quantitative conclusions about the tether’s properties have been drawn from the MT-perpendicular bead excursions.

Theoretical modeling

Simulation of bead fluctuation dynamics. In the TCM assay, the bead–coverslip link is not stationary, as in the traditional TPM assay (1-5). Instead, the bead moves, carried by a motor (Videos 1, 2). Thus, in the stationary system of coordinates, the bead’s trajectory reflects both random bead motion due to thermal noise and its directed transport by the motor (Fig. 1a*).* To take into account the motor’s walking, modeling of the TCM was performed using a moving coordinate system (X’, Y’, Z’), with the origin located on the surface of the MT at the site of motor domain attachment (Fig. 1c). The X’-axis is oriented parallel to the MT pointing toward the plus MT-end. The Y’-axis is perpendicular to the MT and parallel to the coverslip surface, whereas the Z’-axis is perpendicular to the coverslip surface. In our theoretical calculations, this coordinate system moves toward the MT plus-end at 20 µm min^{-1}. Coordinates of the tether-attached bead moving on top of the MT protofilament ($\alpha = 0°$, Fig. 1c) were calculated in the moving coordinate system (Fig. 1d), and then converted into the real bead coordinates (Fig. 1b). Using these coordinates, bead excursions from the motor’s attachment site on the MT were calculated in the MT-parallel (X’-excursions) and MT-perpendicular (Y’-excursions) directions. Histogram distributions of the MT-perpendicular excursions were fitted to Gaussian functions, and their SDs were recorded (Fig. 2 e,f). Note that in real experiments, the velocity of the motor’s walking often changed, and the motor also paused stochastically. Therefore, accurate determination of the MT-parallel excursions is not possible, as described in the section “Plotting the bead clouds”. Therefore, only the MT-perpendicular bead excursions were used to compare theoretical predictions and experimental results (Fig. 2 e,f).

Estimation of the probability of motor binding to different MT protofilaments. A unique aspect of the TCM assay is that the motor can walk on different MT protofilament tracks. A motor is expected to land with equal probability on different protofilaments of an MT suspended in a solution, but landing on a coverslip-attached MT is sterically limited by the motor’s proximity to a coverslip surface, bead diameter and tether’s mechanical properties. Although the exact probability function for such a system is not known, its general shape can be deduced based on simple geometrical considerations. Indeed, the probability of the motor landing on the upper MT protofilaments should be maximal (probability 1 for approximately -25° to 25° range of motor-MT attachment angles, Fig. 1c and Fig. S1). In this range, the bead can easily interact with the MT without bending of the tether. The attachment to the coverslip-bound protofilaments, on the other hand, is impossible (probability 0). Binding is also prohibited to protofilaments located closer than 5 nm (the size of the motor’s head domain) to the coverslip (probability 0 for attachment angles > 130°). For the remaining protofilaments, the probability of motor binding can be assumed to decrease linearly with increasing binding angle, leading to the “simplified” curve in Fig.

S1b. To test the validity of these assumptions for specific tethers, we randomly generated different motor, tether, and bead configurations. The ratio of the sterically possible configurations to the total number of generated configurations was used as a measure of the binding probability for different protofilaments.

Modeling of motions along different MT protofilaments. To simulate the bead's motion during motor walking along different protofilaments, the first segment of the worm-like chain of the connecting tether was tilted at different angles α along the surface of the 25 nm MT cylinder (Fig. 1c), and bead excursions were calculated as described in section "Simulation of the bead fluctuation dynamics". Histograms of the resultant distributions of the MT-perpendicular bead excursions (Fig. S3a) show that for larger angles of motor attachment, the mean bead position deviates from zero, as observed for $\alpha = 0°$ (Fig. S3b, upper graph). The range of bead motion, as measured from the SD of these distributions (Fig. S3b, bottom graph), decreases with increasing angle, and this effect is stronger for a shorter tether. In real experiments, multiple motor runs are sampled, representing different protofilament tracks, encountered by the motor with different probabilities. To model this situation, we combined bead coordinates obtained for different angles (0°–120°) using weight coefficients corresponding to the probability of the motor landing on different MT protofilaments (Fig. S1b). The weight coefficients for short tethers (5–40 nm) were calculated directly, as described in "Estimation of the probability of motor's binding to different MT protofilaments". For longer tethers, the weight coefficients were estimated using the simplified curve in Fig. S1b, which deviates from the calculated curves by < 12%.

Tether modeling. As described in Materials and Methods section in the main text, bead's tether was modeled as a worm-like chain of 2-nm segments. The model included a rule that prohibited penetration of the tether into the bead, MT or coverslip, but the self-avoidance of the tether was not included. Also, we assumed that the first segment of the chain was anchored perpendicularly to the MT surface. These simplifications are justified by our additional analysis of the anchor point flexibility and the tether self-avoidance**.** We determined SD of Y'-excursions using a modified model in which the chain self-avoidance was implemented by introducing additional rule prohibiting individual links to approach each other closer than 2.5 nm (excluding consecutive links, which are by necessity 2 nm apart). The connection point between MT and the first chain segment was also allowed significant flexibility by selecting rotation angles from Gaussian distribution with SD = 17°. The resulting dependencies for these modified models were very similar to those obtained with our simplified model (Fig. S1c), so taking into account these aspects is not necessary. Also, removing the flexibility of the connection point between the last chain link and the bead had no effect on the SD of Y'-excursions for chains with different PLs.

Modeling of increased dsDNA density. Explicit modeling of numerous dsDNA links is computationally intensive, so we used a highly simplified approach to illustrate a possible effect of increased DNA density. Same modeling framework was used as for a single tether, but we additionally assumed that higher link density increased the effective size of the bead by adding a DNA-representing layer (Fig. S3c). Thermal excursions of the bead tethered to a motor via the 215-nm dsDNA tether were calculated as described in "Simulation of the bead fluctuation dynamics", but the motion of the bead's center was constrained by the sum of bead radius and the layer's thickness, which varied from 0 to 150 nm (Fig. S3d). This DNA-representing layer did not restrict the tether's motion, as the tether was allowed to pass freely through it. This modeling framework may underestimate the effect from high DNA density, so directly modeling multiple tethers would likely reveal even smaller bead excursions.

Length of the compound tethers. To estimate the contour lengths of motor tethers based on the amino acid sequences of K560 kinesin-1 construct (6) and TR CENP-E constructs (7), we calculated the total lengths of the predicted coiled-coil segments (probability >90%, calculated with "Coils version 2.2" (8)). The 160 amino acids in the coiled-coil segments of K560 correspond to ~24 nm (0.15 nm per residue (9)), whereas the length of the coiled-coil segment in TR CENP-E is ~8 nm. Taking into account the size of the bead-bound antibody molecule (~ 2 nm), the estimated contour length of the TR CENP-E tether is 10 nm. To estimate the length of the short tether, we summed the lengths of its fibrillar parts: 24 nm of K560 kinesin, 12 nm of dsDNA link (0.34 nm per bp (10)), and ~2 nm of SNAP-GBP, yielding a total length of 38 nm. Because the longest part of this tether is formed by the coiled-coil protein segments, we assumed that this tether had PL = 150 nm (11). The long dsDNA tether had same parts as the short tether, but its 557-bp dsDNA link was 189 nm long, so its total contour length was ~215 nm; the PL of this tether was 46 nm, as in the dsDNA (10).

Supporting Table

Table S1. TCM model parameters.

model parameters	**range of values**
tether contour length	4 - 250 nm
tether persistence length	26, 46, 150 nm
length of tether's segment	2 nm
tether "thickness"	0 nm (2.5 nm in Fig. S1c)
flexibility of tether-MT attachment (SD of angular deviation between the last tether segment and bead's normal vector)	not flexible (0°) (17° in Fig. S1c)
flexibility of tether-bead attachment (SD of angular deviation between the last tether segment and bead's normal vector)	17° (0° in Fig. S1c)
motor angle on MT (corresponding to different protofilaments)	0°, ±30°, ±60°, ±90°, ±120°
radius of the bead	250 nm
diameter of MT cylinder	25 nm

Supporting Figures

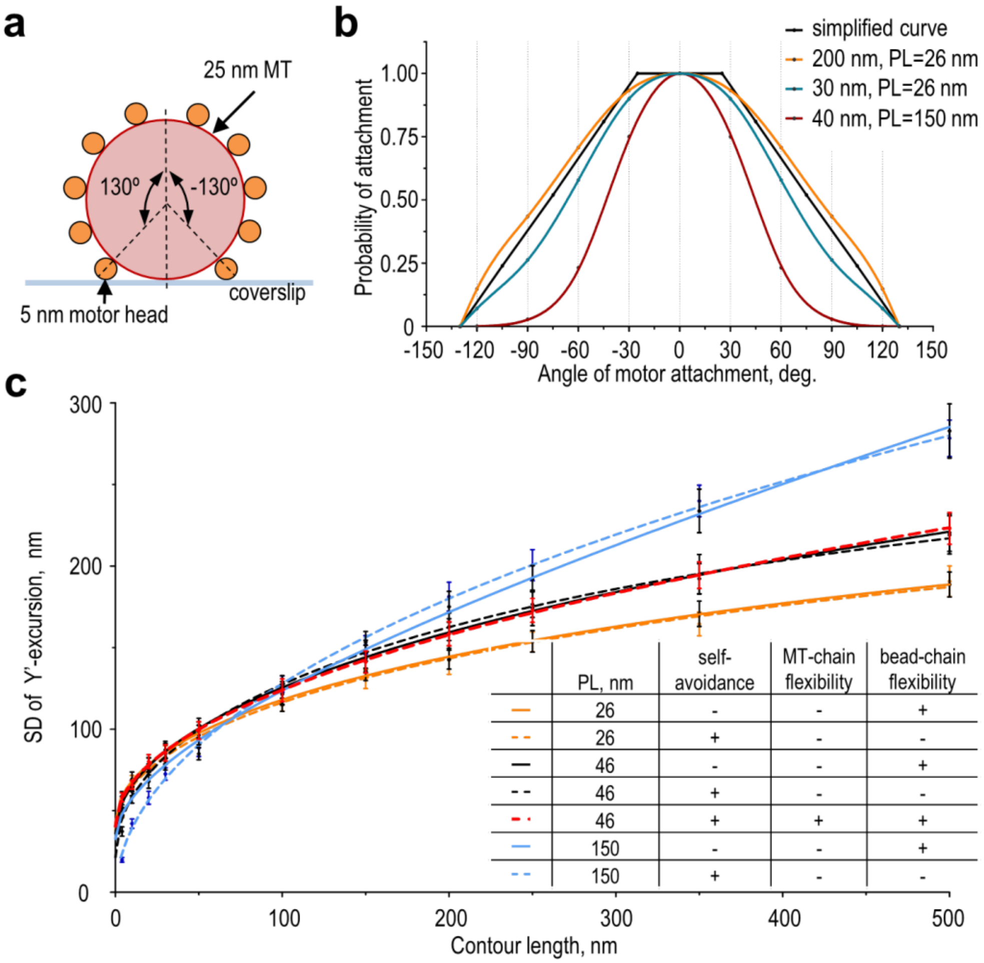

Fig. S1. Geometry of binding of the bead-conjugated motor to the immobilized MT and additional model analyses. (a) Schematic for possible attachment of motor molecules (orange dots) to different protofilaments of the coverslip-immobilized MT cylinder (shown as a cross-section). Protofilaments with attachment angles larger than ±130° are not accessible for motor binding. **(b)** Probability of motor attachment to the MT was calculated for tethers with different contour length and persistence length (PL) as a function of the attachment angle; see Supporting Methods for details. **(c)** Predicted relationship between the SD of Y'-excursions of the bead and contour length for different tethers in TCM assay, see legend to Fig. 1e. Solid lines show same predictions as in Fig. 1e but for a larger range of contour lengths. Broken lines show results for the same model but with a fixed angle of chain attachment to the bead, or for the model in which both ends of the tether were assumed to be flexible and the chain's self-avoidance was implemented (broken red line).

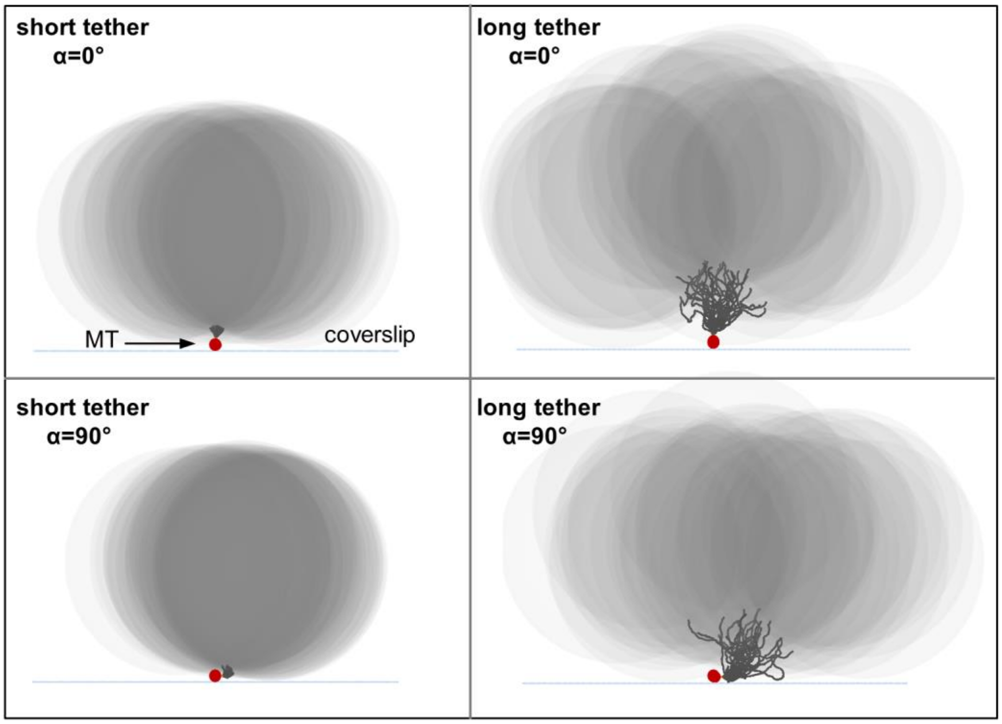

Fig. S2. Impact of the angle of motor-MT attachment on the extent of bead excursions.
Each panel is an overlay of 30 randomly selected frames from Videos 1 and 2, viewed along the MT. Left panels are for the 38-nm tether (as in Video 1), and right panels are for the 215 nm-long tether (as in Video 2); both tethers have PL = 46 nm. Coverslip-immobilized MT is shown in cross-section (red dot), projected bead images as large grey circles, and dsDNA tethers as black lines. The walking motor is in orange, but is almost invisible on this scale. When the motor–MT attachment angle is large ($\alpha = 90^o$, lower panels), the motor walks along the protofilament located close to the coverslips, so bead excursions are more sterically restricted relative to excursions seen with the motor walking on the top MT protofilament ($\alpha = 0^o$, upper panels).

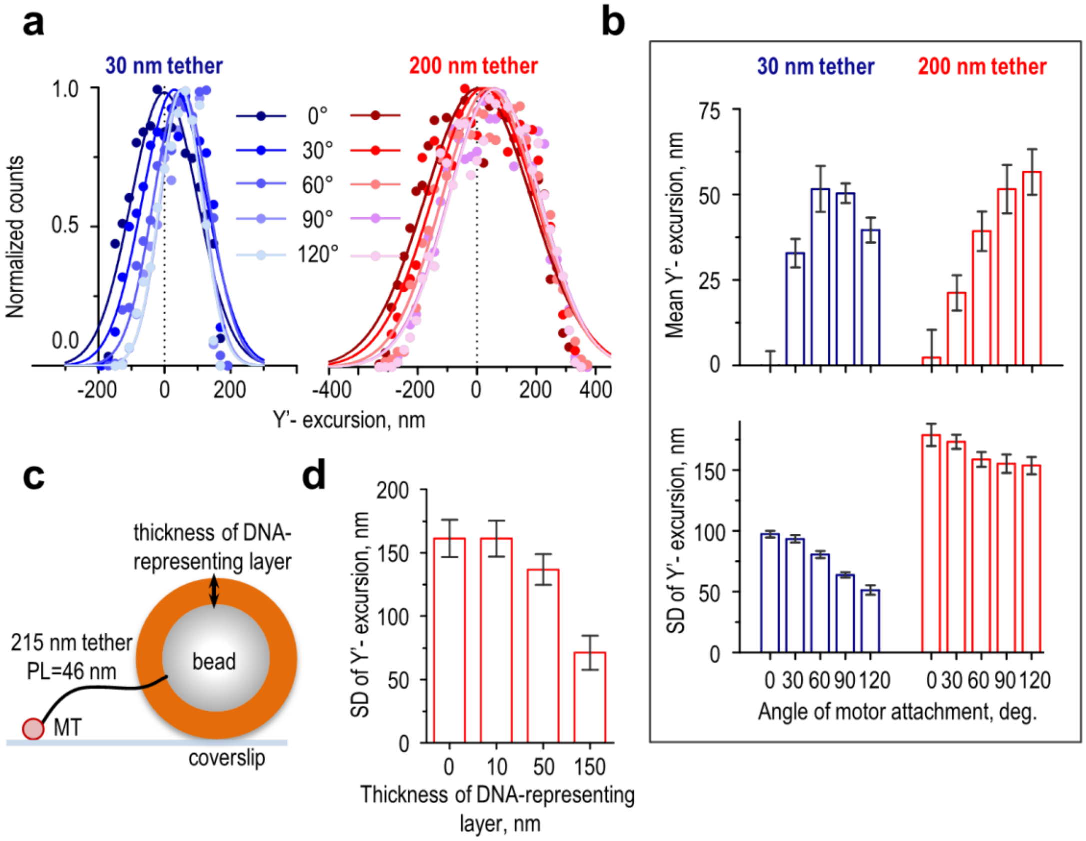

Fig. S3. Additional theoretical analysis of bead excursions. **(a)** Histograms of distributions of MT-perpendicular (Y') bead excursions for indicated angles of motor–MT attachment in the moving coordinate system. Each data set was fit to a Gaussian function and normalized to the mean value. PL = 46 nm; n = 2,000 for each angle. **(b)** Predicted Y'- excursion mean and SD for distributions in panel **a**. Bars are SEMs (top graph) or standard errors (bottom graph) for the Gaussian fits. **(c)** Schematic for modeling bead excursions in the presence of multiple DNA tethers, represented with a layer that constrains bead motions near the coverslip. **(d)** Theoretically predicted SD of MT-perpendicular (Y') bead excursions in the presence of the DNA-representing layers; see Supporting Methods. Error bars are as in Fig. 1e.

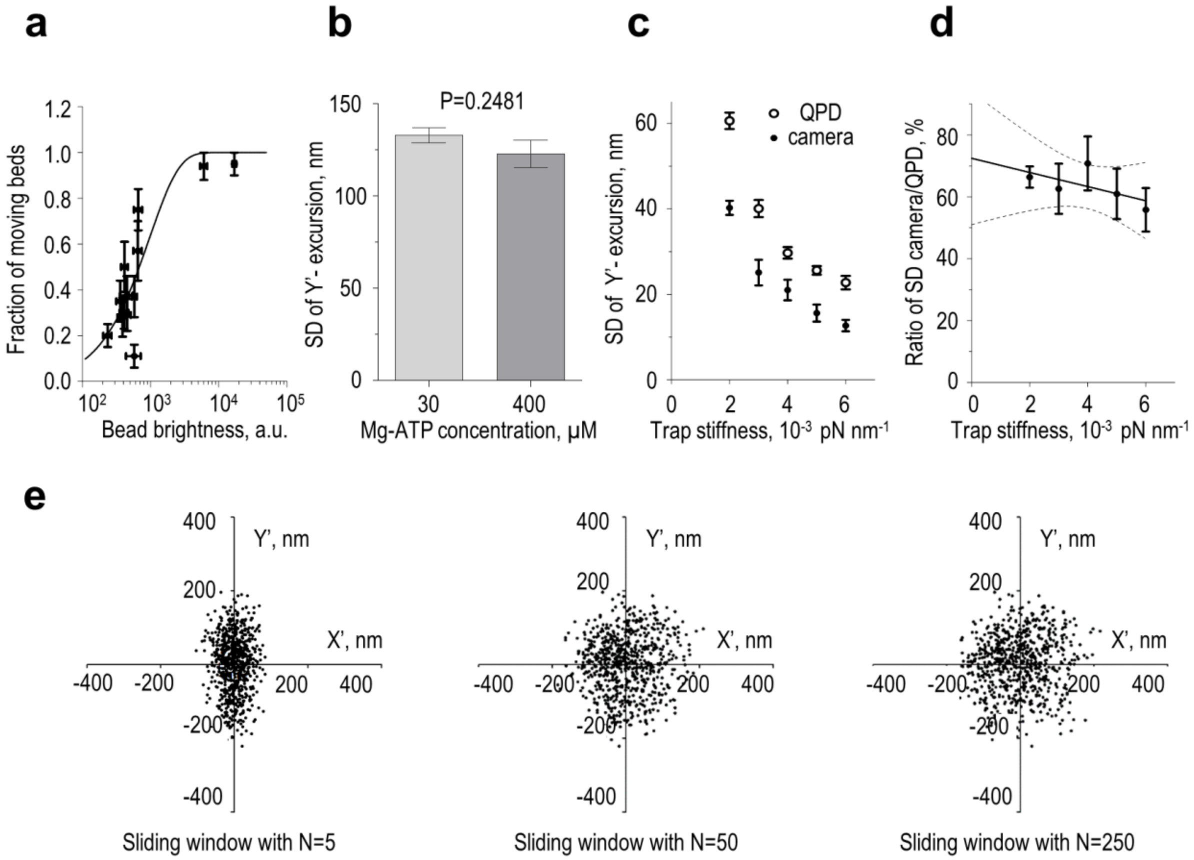

Fig. S4. Additional features of the TCM assay. **(a)** Fraction of moving beads as a function of coating density, as calculated from kinesin-1–GFP fluorescence intensity. Kinesin-1–GFP was conjugated with long dsDNA tethers. Each data point represents average brightness of ~100 beads from one preparation; percent of moving beads in each preparation was determined by examining ~20 beads. Error bars are SEMs. **(b)** SD of MT-perpendicular (Y') bead excursions in motility experiments with kinesin-1–GFP conjugated via long dsDNA links at two Mg-ATP concentrations. Error bars are SEMs based on 40 beads for 30 μM Mg-ATP or 16 beads for 400 μM Mg-ATP. P-value was determined by two-tailed unpaired t-test. **(c)** SD of bead excursions a function of trap stiffness. Error bars are SEMs. Beads were held in a laser trap, and their coordinates were recorded simultaneously with a CCD camera (10 ms exposure) and QPD (100 kHz). To remove background noise from the QPD amplifier, QPD data are shown after subtraction of the signal obtained in a trap with high stiffness (0.05 pN nm^{-1}). Data are based on 3–5 beads for each stiffness. **(d)** Ratio of SD of bead excursions obtained with a CCD camera to the SD for the same beads recorded by QPD (see panel **c**). Points are mean ± SEM, and the line indicates the results of linear regression (with 95% confidence band). **(e)** Experimental cloud plots for bead excursions obtained for the same bead trajectory, but prepared using different sliding windows that average the MT-parallel component (see Supporting Methods, “Plotting the bead clouds”).

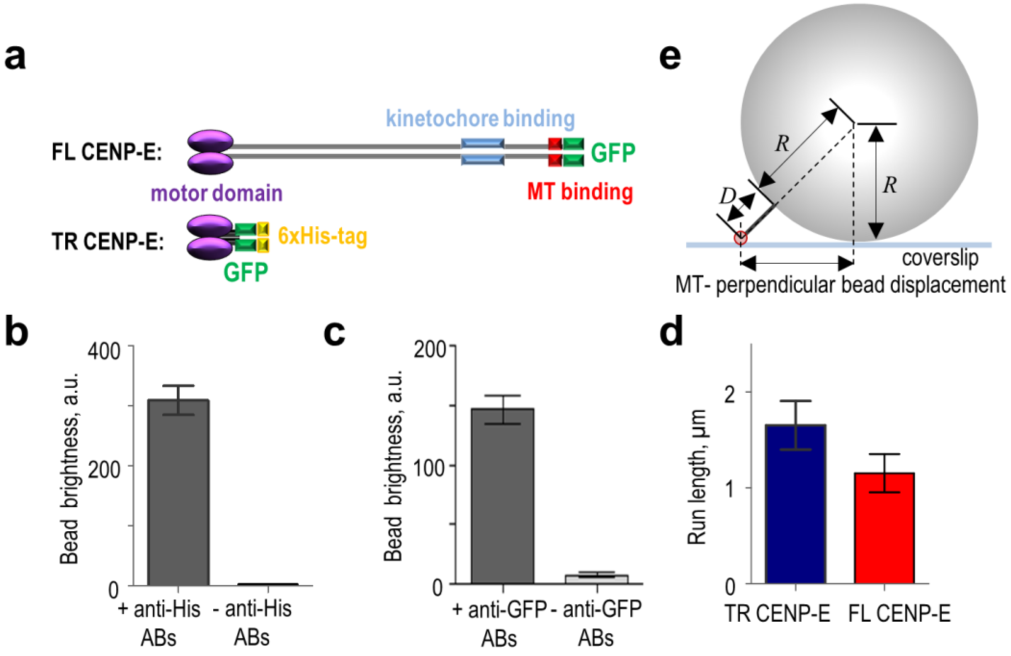

Fig. S5. Supplemental information for experiments with CENP-E. (a) Schematics of the CENP-E proteins used in our assays. **(b)** Brightness of beads coated or not with anti-His antibodies, followed by incubation with TR CENP-E protein tagged with 6His and GFP. Mean ± SEM, n = ~100 beads per sample. **(c)** Brightness of beads coated or not with anti-GFP antibodies, followed by incubation with FL CENP-E protein tagged with GFP. Mean ± SEM, n > 30 beads per sample. **(d)** Run lengths for CENP-E-coated beads. Data are means ± SEM measured for 21 and 18 beads for TR and FL CENP-E, respectively. **(e)** Schematic explaining the relationship between *D* (distance from the surface of the bead with radius *R* to the coverslip-attached MT (cross-section is shown) and the MT-perpendicular displacement of the bead.

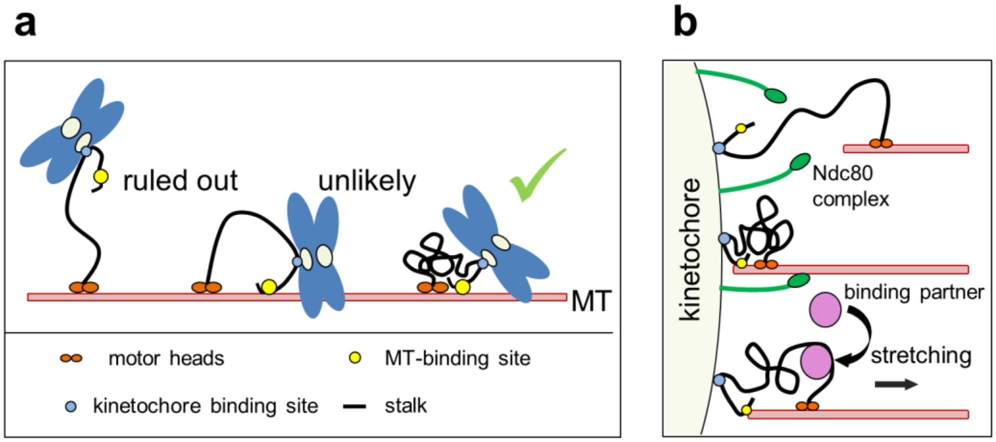

Fig. S6. Implications for kinetochore-MT tethering via CENP-E kinesin. (a) Dynamic CENP-E stalk configurations. Our TCM experiments argue against a model in which the discontinuous coiled-coil stalk of the transporting CENP-E kinesin is extended. The experiments with sideways force suggest that the MT-bound CENP-E is compactly folded. **(b)** Illustration of various CENP-E configurations during mitosis. Early in mitosis, elongated CENP-E may help contact MTs as far as 200 nm away from the kinetochore. However, if CENP-E remains elongated, the kinetochore-associated MT-binding proteins like Ndc80 (shown in green) would not be able to reach the MT (top image). We hypothesize that the compact configuration of CENP-E allows for a shorter distance between the kinetochore and the MT tip, enabling MT-end binding by other kinetochore proteins (center image). Variable tension transduced by the compact CENP-E stalk and causing its partial extension could modulate its binding to various kinetochore partners, thereby mediating a tension-dependent kinetochore response (bottom image).

Video legends

Video 1. Theoretical simulation of a bead attached to a walking motor via a 30-nm tether. The bead-bound motor moves along the coverslip-attached MT (red) in 8-nm steps at 20 µm min^{-1} (one step per frame). The 30-nm tether was modeled as a worm-like chain with PL = 46 nm, similar to the persistence length of dsDNA. Played at 21 fps, the motion appears 2-fold slower than in the model. Bead (0.5 µm in diameter), MT, and tether are drawn to scale.

Video 2. Theoretical simulations of a bead attached to a walking motor via a 200-nm tether. Calculations were performed as for Video 1, but with a 200-nm tether.

Video 3. TCM experiment with a bead moving along a coverslip-immobilized MT. This 0.5-µm bead was coated with 215-nm dsDNA links and kinesin-1 at low density, so its motion is likely to be driven by a single motor. After the bead binds to the MT, it moves along the MT track for ~6 µm until it detaches. Recording was made by DIC with 10-ms exposures, and is played at 100 fps. Scale bar is 2 µm. The MT image was captured separately with 100-ms exposures and overlaid on bead images to achieve better visualization of the MT.

Video 4. Illustration of bead motion relative to the MT in sideways force experiments. The bead (0.5 µm diameter) moves along the coverslip-attached MT (red) in 8-nm steps at 20 µm min^{-1} (one step per frame). Optical trap drives bead oscillations at 1 Hz perpendicular to the MT with an amplitude of 1 µm. Played at 21 fps, the motions appear 6-fold slower than in the model.

Supporting References

1. Brinkers, S., H. R. C. Dietrich, F. H. de Groote, I. T. Young, and B. Rieger. 2009. The persistence length of double stranded DNA determined using dark field tethered particle motion. J Chem Phys 130(21):215105.
2. Han, L., B. Lui, S. Blumberg, J. Beausang, P. Nelson, and R. Phillips. 2009. Calibration of Tethered Particle Motion Experiments. In Mathematics of DNA Structure, Function and Interactions. C. J. Benham, S. Harvey, W. K. Olson, D. W. Sumners, and D. Swigon, editors. Springer New York. 123-138.
3. Nelson, P. C., C. Zurla, D. Brogioli, J. F. Beausang, L. Finzi, and D. Dunlap. 2006. Tethered particle motion as a diagnostic of DNA tether length. J Phys Chem B 110:17260-17267.
4. Pouget, N., C. Dennis, C. Turlan, M. Grigoriev, M. Chandler, and L. Salomé. 2004. Single-particle tracking for DNA tether length monitoring. Nucleic Acids Research 32:e73-e73.
5. Towles, K. B., J. F. Beausang, H. G. Garcia, R. Phillips, and P. C. Nelson. 2009. First-principles calculation of DNA looping in tethered particle experiments. Physical biology 6:025001.
6. Case, R. B., D. W. Pierce, N. HomBooher, C. L. Hart, and R. D. Vale. 1997. The directional preference of kinesin motors is specified by an element outside of the motor catalytic domain. Cell 90:959-966.
7. Kim, Y., J. E. Heuser, C. M. Waterman, and D. W. Cleveland. 2008. CENP-E combines a slow, processive motor and a flexible coiled coil to produce an essential motile kinetochore tether. Journal of Cell Biology 181:411-419.
8. Lupas, A., M. Van Dyke, and J. Stock. 1991. Predicting coiled coils from protein sequences. Science 252:1162-1164.
9. Alberts, B., A. Johnson, J. Lewis, D. Morgan, M. Raff, K. Roberts, P. Walter, J. Wilson and T. Hunt. 2015. Molecular Biology of the Cell, 6th edition: Ch3. “Proteins: The Shape and Structure of Proteins”, p. 116. Garland Science, Taylor and Francis Group, New York , United States.
10. Wang, M. D., H. Yin, R. Landick, J. Gelles, and S. M. Block. 1997. Stretching DNA with optical tweezers. Biophysical journal 72:1335-1346.
11. Wolgemuth, C. W., and S. X. Sun. 2006. Elasticity of alpha-helical coiled coils. Physical review letters 97:248101.